

1 **Waves and wrecks: A computational fluid dynamic**

2 **study in an underwater archaeological site**

3 Fernández-Montblanc, T.^a, Izquierdo, A.^b, Quinn, R.^c, Bethencourt, M.^d

4 ^a Department of Applied Physics, International Campus of Excellence of the
5 Sea (CEI·MAR), University of Cádiz, Avda. República Saharaui s/n, 11510,
6 Puerto Real, Cádiz, Spain. tomas.fernandez@uca.es. (Corresponding author)

7 ^b Department of Applied Physics, International Campus of Excellence of the
8 Sea (CEI·MAR), University of Cádiz, Avda. República Saharaui s/n, 11510,
9 Puerto Real, Cádiz, Spain. alfredo.izquierdo@uca.es.

10 ^c School of Environmental Sciences, Ulster University, Coleraine, BT52 1SA,
11 Northern Ireland. rj.quinn@ulster.ac.uk.

12 ^d Department of Materials Science, Metallurgy Engineering and Inorganic
13 Chemistry, International Campus of Excellence of the Sea (CEI·MAR),
14 University of Cádiz, Avda. República Saharaui s/n, 11510, Puerto Real, Cádiz,
15 Spain. manuel.bethencourt@uca.es.

16

17 **Abstract**

18 The modification of waves by shipwrecks and the resulting scour play
19 important roles in shipwreck site formation, and conservation of
20 archaeological sites. The oscillatory flow induced by waves and its
21 interaction with the hull structure at a historic shipwreck site was analyzed
22 using a two phase 2D model based on the Reynolds averaged Navier-Stokes
23 equations and shear stress transport (SST) k-Omega turbulence model,
24 with inputs from field-based bathymetric survey. The relative importance

25 and seasonal variation in hydrodynamic processes were investigated (flow
26 velocity increase, coherent structures and vortex shedding, turbulence and
27 steady current induced by the non linearity of waves). Results demonstrate
28 that frictional velocity and flow increase dominate morphological change in
29 the low wave energy period (LEP), whereas turbulent shear stress and large
30 coherent structures dominate scouring in the high wave energy period
31 (HEP). Furthermore, flow acceleration around the hull structure and
32 recirculation cells originated by wave non-linearities become more
33 prominent in the HEP, modifying the trajectory of the shedding vortex and
34 increasing its capacity to transport sediment. The results demonstrate, for
35 the first time, that computational fluid dynamics is a valuable tool in
36 assessing the wave structure interaction in full scale and realistic
37 morphological conditions at complex shipwreck sites.

38 **Keywords:** Computational fluid dynamics; Multi-beam echo-sounder;
39 Shipwreck; Site formation processes; Hydrodynamics; scouring

40 **1 Introduction**

41 In the last decades, advances in technology have led to the development,
42 exploitation and exploration of the seabed resulting in the discovery of a
43 considerable number of shipwrecks and other archaeological sites
44 (Besrgstrand and Godfrey, 2007). Simultaneously, marine environmental
45 conditions and their relationship to underwater cultural heritage (UCH) have
46 provoked considerable interest due to the direct link to the status of
47 underwater cultural heritage and the perspective of conservation *in situ*
48 (Leino, 2011; Wheeler, 2002). In particular, physical processes have been
49 proposed by various authors as dominant in early stages of site formation

50 (Quinn, 2006; Ward et al., 1999), and the coupling between water and
51 sediment dynamics controlling the sediment budget is considered as
52 fundamental in site formation studies (Smyth and Quinn, 2014).

53 Quantifying sediment budgets at wreck sites is important, as sediment
54 offers physical stability to shipwrecks, and the deposition and erosion of
55 sediment at sites modifies the geochemical characteristics which control
56 chemical degradation and the biological activity influencing the decay of
57 UCH materials (Ruuskanen et al., 2015; Ward, 1999).

58 Sediment budgets at shipwreck sites depend on the sediment availability
59 and characteristics, the hydrodynamic regime, and its interaction with the
60 shipwreck structure. Scour takes place when an obstacle modifies the flow
61 pattern in its immediate neighbourhood causing an increase in local
62 sediment transport. Given the importance of scour in the sediment budget
63 around shipwrecks and in site formation and conservation studies, the
64 scouring process has received increased attention from the scientific
65 community in the last decade (e.g. Astley et al., 2016; Baeye et al., 2016;
66 Fernández-Montblanc et al., 2016; Smyth and Quinn, 2014; Quinn, 2006;
67 Quinn and Smyth, in press).

68 Thus, several research projects have focused on understanding shipwrecks
69 under steady flow conditions, including sediment dynamics and associated
70 scour pit formation. These studies used different data and methodologies,
71 and can be subdivided by type into accretion-erosion models (Astley et al.,
72 2016; Bates et al., 2011; Quinn and Boland, 2010), scaled physical models
73 (Saunders, 2005) and computational fluid dynamics (CFD) models in
74 combination with high resolution multibeam echosounder bathymetric data
75 (Smyth and Quinn, 2014; Quinn and Smyth, in press).

76 However, the fate of shipwrecks dominated by oscillatory flow and
77 associated scouring has been considerably less studied. A real-world case
78 study of shipwreck scouring under shoaling waves based on side scan sonar
79 data is outlined in Quinn (2006). The burial-exposure of different artefacts
80 in an archaeological context is described in McNinch et al. (2006) using
81 numerical modelling, calibrated by sediment and hydrodynamic
82 observations. More recently, wave propagation and hydrodynamic modelling
83 in combination with time-lapse bathymetric surveys and hydrodynamic
84 measurements was used to characterize scour and seasonal
85 morphodynamic changes in an energetic shallow water shipwreck site where
86 part of the hull has been preserved (Fernandez-Montblanc et al., 2016).
87 Conversely, the scouring due to wave and obstacle interaction has been
88 widely studied in other scientific fields such as coastal engineering, with
89 applications to breakwaters (Sumer et al.; 2001, 2005, Young and Testik,
90 2009), pipelines and mines (Mattioli et al., 2013; Sumer, 1990; Voropayev,
91 et al., 2003), or offshore structures mounted on the seabed (Nielsen,
92 2012). As a result, scouring can be estimated through simple empirical
93 equations. However, those studies have been performed usually assessing
94 the flow interaction with relative simple geometries, as those are commonly
95 used in coastal and offshore engineering. The majority of these studies are
96 based on scaled physical models with inherent limitations. Therefore, due to
97 its importance in site formation and *in-situ* conservation of UCH, there is a
98 need to further investigate the oscillatory flow interaction with complex
99 geometrical structures (i.e. shipwrecks). It is important for these models to
100 incorporate real and complex morphological scenarios to reflect those found
101 in nature, and to use field data to calibrate and validate them.

102 In this context, CFD represents a reliable and cost-effective way of
103 calculating the flow pattern around complex geometrical structures.
104 Increasing computing power and resulting simulation efficiency allows the
105 application of CFD to large domains representing complex three dimensional
106 seabed structures, natural or man-made, where the scour and
107 morphodynamic behaviour are associated with near-bed turbulent flow. This
108 study focuses on the application of CFD to investigate the interaction
109 between a historic shipwreck and wave-induced oscillatory flow, with the
110 aim of assessing the relative importance of different mechanisms that
111 originate and control scouring in these environments. CFD modelling is
112 validated with field-based hydrodynamic data.

113

114 **2 Theoretical background**

115 An object placed on the seabed changes the flow pattern in the immediate
116 vicinity. Changes may result in flow contraction, promoting streamline
117 convergence and flow acceleration, vortex formation around the structure
118 (with or without vortex shedding behind the structure), increased
119 turbulence, and modification of wave characteristics (occurrence of
120 reflection and diffraction or breaking). As a result, shear stress is increased
121 on the seabed, promoting sediment transport around the object and leading
122 to scour (Sumer and Fredsøe, 2002). The process continues until a new
123 quasi-equilibrium state is reached, in which the increase in bed shear stress
124 due to the presence of the structure is balanced as a direct consequence of
125 depth increment and/or the loss of fine sediment in the scoured area. If the
126 eroding seabed is composed of fined-grained (clay-silt) material, suspension

127 transport carries the sediment far away from the structure (Whitehouse et
128 al., 2011b), but if the seabed is composed of coarse-grained (sand-gravel)
129 sediment, the sediment is deposited near the structure (Smyth and Quinn,
130 2014).

131 Oscillatory flow adds time-dependence to the above phenomena. The wave
132 boundary layer, horizontal and vertical velocity changes, turbulence, and
133 the large coherent structures (LCS) formed around the object vary along a
134 wave cycle. Studies on oscillatory flow around submerged breakwaters and
135 horizontal cylinders on the seabed indicate that the flow pattern and scour
136 are mainly controlled by the Keulegan-Carpenter (KC) number (Vorapayev,
137 2003):

$$138 \quad KC = 2\pi a/D,$$

139 where D is the characteristic length of the object (i.e. diameter for a
140 cylinder), $a = U_{mo}T/2\pi$ is the amplitude of the free stream motion, and T is
141 the wave period. Sumer (1991) analysed the vortex dynamics around a
142 horizontal cylinder on the wall at high Reynolds (Re) numbers (mostly at
143 $Re \sim 10^5$):

$$144 \quad Re = U_{mo} D / \nu,$$

145 where ν is the kinematic viscosity of water and U_{mo} the maximum value of
146 the free stream velocity. Sumer (1991) found that for small values of KC no
147 flow separation occurs. However, increasing KC to 4 promotes flow
148 separation and symmetrical vortex formation upwave and downwave of the
149 cylinder, and for $4 > KC > 7$, asymmetry in the formation and motion of the
150 vortices is introduced into the system. At $KC > 7$, vortex shedding occurs.

151 Similar results were found in a physical experiment with sinusoidal forcing

152 at $Re=300-500$, carried out by Testik et al. (2005). They found horseshoe
153 vortices of opposite rotation formed periodically on both sides of the
154 cylinder. For $KC = 8.4$, the vortex formed on each side washed over the
155 cylinder in the following half cycle and formed a vortex pair with the initial
156 one (with the opposite vorticity sign) and shed away periodically as a paired
157 structure. In the case of physical experiments forced with waves, instead of
158 sinusoidal forcing, no shedding of the paired structure was found in
159 experiments with $7 > KC > 23$ and Re ranging from $3 \cdot 10^3$ to $2.6 \cdot 10^4$ (Mattioli
160 et al., 2013). Investigations on scour around vertical piles exposed to waves
161 have shown the increment in bed shear stress due to horseshoe vortex
162 development, especially in the turbulent bottom boundary layer (Sumer et
163 al., 1997). Although the onset of scour is related to the lee-wake vortex and
164 vortex shedding, flow sweeps the sediment into the core and the shedding
165 vortex carries the sediment away from the pile as it is advected
166 downstream (Sumer et al., 1993). A more recent scour study around a half-
167 buried sphere under steady flow showed that the increase in turbulence
168 beneath the horseshoe vortex enhances bed shear stress amplification and
169 has a notable contribution to the scour (Dixen, 2013).

170 In addition, the steady current generated by nonlinear effects induced by
171 waves results in a secondary flow in the form of steady streaming and
172 undertow. The steady streaming flow generated by wave propagation over
173 the structure is the result of the non-uniform oscillatory action in presence
174 of the structure. Its relevance in the scouring process has been revealed for
175 a vertical pile and oscillatory flow (Sumer and Fredsoe, 2001) and in a
176 submerged breakwater (Sumer et al., 2005). Steady streaming $O(10^{-1} \text{ m}\cdot\text{s}^{-1})$
177 transports and redistributes the sediment that the oscillatory flow $O(10^0$

178 m·s⁻¹) brings into suspension. Also the non uniformity in vertical
179 distribution of spanwise velocity generates a steady flow known as
180 undertow; a gravity driven current with the maximum located near the
181 seabed and oriented seaward. Undertow is induced by two mechanisms: (1)
182 rollers that carry water shoreward in the upper water column under
183 breaking conditions, and (2) eulerian drift in the case of non-breaking
184 conditions.

185 Finally, various authors have noted the increment in sediment transport
186 produced by turbulence, whether internally generated turbulence (Nelson,
187 1995), or externally generated due to flow structure-interaction (Sumer,
188 2003). The turbulence makes the transport of momentum more effective
189 (as well as mass and energy) between fluid layers (Dixen, 2013) with a
190 consequent increment in sediment transport. In addition, turbulence
191 promotes the settling delay (Murray, 1970), which favours the sediment
192 transport in suspension and increases scour.

193 All near wall processes and characteristics, such as the boundary layer
194 structure, thickness, the point of vortex and flow separation, friction
195 velocity and turbulence are conditioned by the roughness of the seabed
196 (sand-grain and bed form roughness) and the roughness characteristics of
197 the of the obstacle.

198 **3 Methodology**

199 **3.1 Study site**

200 *Fougueux*, a 74-gun Temeraire-class French ship-of-the-line, took part in
201 the Battle of Trafalgar in October 1805, where the British fleet defeated the
202 combined French-Spanish fleet off the coast of Cádiz. *Fougueux* was

203 wrecked after the battle, when she was driven onto a rocky shoal. The
204 wreck site is characterized by low to moderate wave energy conditions, with
205 the exception of high the energetic winter storms from WSW. Partial burial
206 in sediment has resulted in the preservation of a considerable portion of the
207 wooden hull structure (15x7m²) along with 31 cannons and a large anchor
208 (Rodríguez Mariscal et al., 2010).

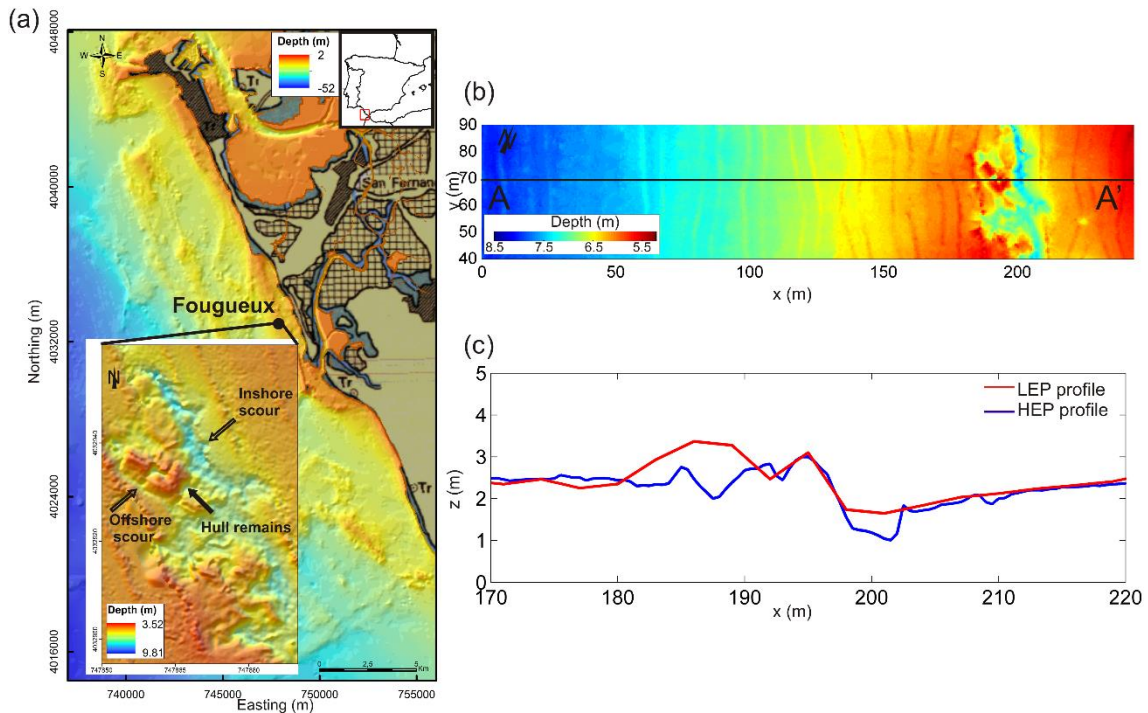
209 The *Fougueux* wreck site is located on the south-western seashore of the
210 Iberian Peninsula (Gulf of Cádiz), in a shoal seaward of the Sancti Petri sand
211 spit (Figure 1a). The seafloor around the wreck is gently sloping from 5-10
212 m depth (Figure 1a), and comprises unconsolidated well-sorted fine quartz
213 sand ($D_{50}=1.8 \cdot 10^{-4}$ m) with bedrock areas where Plio-quadernary shelly
214 conglomerate crops out (Gracia et al., 2008). The scattered wreck remains
215 are located in an energetic shallow-water environment, where wave
216 oscillatory flow promotes scouring resulting in inshore pits (maximum depth
217 of 0.77 m) scoured deeper than offshore pits (0.35 m depth) (Figure 1a).
218 Seasonal changes are observed, showing accretion during a low wave-
219 energy period (LEP) from May to September and net erosion around the hull
220 structure during a high-energy period (HEP) from November to April
221 (Fernández-Montblanc et al., 2016). At the deepest point at the centre of
222 the wreck site ($x \sim 192$) minor seasonal variations were found (Figure 1a
223 and Figure 1c). The mean wave height at the site is 0.67 m during LEP and
224 1.18 m in HEP, whereas the maximum wave height is 4 m, and is limited by
225 local depth. Mean bottom orbital velocity fluctuates from $0.30 \text{ m} \cdot \text{s}^{-1}$ during
226 LEP to $0.68 \text{ m} \cdot \text{s}^{-1}$ during HEP. The maximum value of near-bed wave orbital
227 velocity, calculated by a wave propagation model, rises to $2 \text{ m} \cdot \text{s}^{-1}$ during
228 winter storms. The area is meso-tidal (mean tidal spring range of 2.96 m),

229 with a dominant semidiurnal tidal variability. Peak currents are orientated
230 NNW and SSE at flood and ebb tide conditions respectively, with mean
231 values 0.15-0.25 m·s⁻¹. Velocities above this value, directed NNW,
232 correspond to a SE wind. In contrast, current velocities greater than 0.25
233 m·s⁻¹, directed SSE, are related to wind drift (Fernández-Montblanc et al.,
234 2016).

235 **3.2 Field data**

236 ***Bathymetric data***

237 In order to collect bathymetric data corresponding to the low energy wave
238 period (LEP; summer conditions) and high energy wave period (HEP; winter
239 conditions), two successive surveys were conducted. The LEP survey was
240 performed on 11.09.2013 using an Ohmex Sonarmite v3.0 singlebeam
241 echosounder operating at 235 kHz (sample rate 1 Hz and theoretical vertical
242 resolution 0.05 m). A HEP survey was conducted on 23.11.2013, using a
243 Reson Seabat 8124 multibeam echosounder operating at 200 kHz (1.5°
244 beam width, 0.01 m vertical resolution and 39.89 Hz sample rate). In both
245 cases, positional data were acquired using an RTK-GPS Leica 1200, from
246 which tidal and wave corrections were taken. Two digital elevation models
247 were derived from the LEP and HEP surveys, and two 250 m long
248 bathymetric profiles (AA') were extracted and used as a bottom boundary in
249 the CFD study (Figure 1b, Figure 1c).



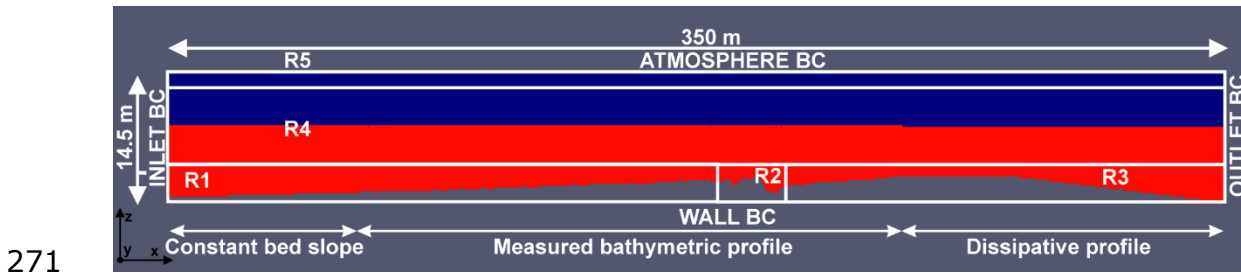
250

251 Figure 1. (a) Location map of the study site in the Gulf of Cadiz and detail of the
 252 *Fougueux* site from the multibeam bathymetric data. (b) Location of bathymetric
 253 profile in multibeam bathymetry. (c) Detail of bathymetric profiles corresponding to
 254 LEP and HEP at the *Fougueux* site.

255 3.3 CFD study

256 The CFD modelling of the *Fougueux* site was performed using OpenFOAM ®
 257 software, an open source toolbox that allows users to solve problems of
 258 turbulence and complex fluid flows using finite volume discretization. The
 259 InterFoam solver was employed in this study, solving the three-dimensional
 260 Reynolds averaged Navier-Stokes equations for two incompressible phases
 261 (sea-water and air in our case represents a free surface flow solver) using a
 262 finite volume discretization and the volume of fluid method. Flow turbulence
 263 is represented by a two-equation SST K-Omega model (Menter, 1994). This
 264 model combines the use of a k-epsilon turbulence model in the free flow
 265 regions and a k-omega turbulence model inside the boundary layer, avoiding
 266 the problem of the high sensitivity to the inlet boundary condition of the k-
 267 omega model (Bozorgnia et al., 2014). IHFoam was used to implement the
 268 boundary conditions for wave generation and absorption, reducing the

269 problem of reflexion in the boundaries without an extension of the domain
270 (Higuera et al., 2013).



271
272 Figure 2. Computational domain used in numerical simulation along with boundary
273 conditions (BC).

274 The numerical experiments were carried out in a full scale 2D computational
275 domain, measuring 350.0 x 14.5 m² and the reference system was set as
276 illustrated Figure 2. The reference system was placed at the furthest point
277 offshore (A) (Figure 1b). The x axis is positive in the wave propagation
278 direction (AA') Figure (1b). The z axis for the domain was located at the
279 deepest point furthest offshore, being positive upward (Figure 1c). The
280 model domain was subdivided into regions with different resolutions to
281 reduce the number of cells and computational time (Figure 2). Region R4,
282 where wave propagation takes place, has cell sizes of $\Delta x = 0.10$ m and
283 $\Delta z = 0.05$ m. Region R1 and R3 have cell sizes of $\Delta x = 0.10$ m and Δz varying
284 from 0.02 m at bottom to 0.10 m at top. Region R2, where the wreck-wave
285 interaction is focused, comprises an unstructured prismatic mesh of 0.005
286 m cell size, allowing the mesh to adapt to the complex geometry of the
287 wreck. The smooth changes in mesh resolution in the transition areas (R1-
288 R2 and R2-R3) reduces the drastic changes in the near surface boundary
289 flow. The friction coefficient at the seafloor was set as uniform in the whole
290 domain as a rough wall function dependent on Nikuradse roughness length
291 (k_s). A grain size value of $D_{50} = 1.8 \cdot 10^{-4}$ m from measurement on five

292 sediment samples collected at the shipwreck site was used to calculate a k_s
293 $= 4.5 \cdot 10^{-4} \text{m}$ using the relation proposed by Soulsby (1997) for a flat bed
294 ($k_s \sim 2.5 \cdot D_{50}$). Water density was set equal to 1025 kgm^{-3} corresponding to
295 20°C and 35 PSU salinity. Air density was taken as 1 kgm^{-3} . The surface
296 tension in the air-water system was given a value of 0.07 kgs^{-2} . Numerical
297 simulations were run in parallel on a high performance computing facility
298 using 32 processors (2.6 GHz), of 2 CPUs subdividing the domain into 32
299 subdomains. During the simulation, a variable time step was specified with
300 a Courant number lower than 0.5 ensuring numerical stability.

301 Table 1 outlines the numerical experiments conducted in the study. Five
302 different wave conditions typical of the *Fougueux* site were simulated using
303 the two bathymetric settings (LEP and HEP). In the first pair of simulations,
304 a case representing mean storm conditions in the area (E1_HEP and
305 E1_LEP) was run. The second pair represents the response to a fading
306 storm (E2_HEP and E2_LEP). Swell wave conditions were simulated for
307 experiment 3 (E3_HEP, E3_LEP), and wave breaking conditions for
308 experiment 4 (E4_HEP, E4_LEP). Finally, a simulation of offshore wave
309 breaking was conducted (E5_HEP, E5_LEP).

310 Assuming that wave propagation takes place along the x axis which is
311 perpendicular to the shoreline (Figure 1a and Figure 1b), the set of wave
312 parameters (wave phase, wave height and wave periods) were used as
313 inputs at the inflow boundary location (Inlet BC) (Figure 2). IHFoam was
314 used to realistically generate waves at Inlet BC according to different wave
315 theories (see Higuera et al. (2013) for further details). In this set of
316 numerical experiments E1_LEP and E1_HEP were conducted using Stokes II

317 theory, and cnoidal theory was used for the rest of the experiments,
 318 according to the range proposed by Le Méhauté (1976).

Wave characteristics					Bathymetry		Water level
Name	Wave type	H (m)	T (s)	Wave Conditions	HEP	LEP	Depth(m) on hull Remains(x=195m)
E1_LEP	Regular	1.5	6	Mean Storm conditions		X	5.52
E1_HEP	Regular	1.5	6	Mean storm conditions	X		5.52
E2_LEP	Regular	3.0	9	Fading storm		X	6.84
E2_HEP	Regular	3.0	9	Fading storm	X		6.84
E3_LEP	Regular	2.4	15	Swell wave conditions		X	5.52
E3_HEP	Regular	2.4	15	Swell wave conditions	X		5.52
E4_LEP	Regular	3.5	15	Wave breaking		X	5.52
E4_HEP	Regular	3.5	15	Wave breaking	X		5.52
E5_LEP	Regular	4.0	9	Offshore wave breaking		X	5.52
E5_HEP	Regular	4.0	9	Offshore wave breaking	X		5.52

319 Table 1. Wave characteristics, bathymetric conditions and water depth used
 320 in the numerical experiments.

321 **3.4 Data analysis**

322 The modelled time series of the horizontal and vertical velocity components
 323 in all grid nodes were processed to extract the mean and fluctuating terms
 324 from instantaneous data, according to

$$325 \mathbf{u}(x, z, t) = \bar{\mathbf{u}}(x, z, t) + \mathbf{u}'(x, z, t); \quad (1)$$

326 where \mathbf{u} is the instantaneous velocity, $\bar{\mathbf{u}}$ is the mean (steady) component
 327 and \mathbf{u}' is the fluctuating (turbulent) component of the instantaneous
 328 velocity. Several methods can be applied to separate the mean and
 329 turbulent components from an instantaneous velocity (Longo, 2002). These
 330 methods include high-pass filtering (Sawamoto et al., 1982), phase
 331 averaging (Ting and Kirby, 1996), moving phase averaging (Nadaoka, 1989;
 332 Standy and Feng, 2005), ensemble averaging (Chang and Liu, 1999) and
 333 differencing method (Scott et al., 2005). In the commonly used phase and

334 moving phase methods, the wave breaking variation from wave to wave can
335 affect the accuracy of averaging results (Chang and Liu, 1999). Therefore,
336 and considering the high repeatability of the flow field, the ensemble
337 averaging method was applied. To that end the time series of instantaneous
338 velocity (\mathbf{u}) was divided into wave cycles by applying the zero up crossing
339 method from the free surface elevation signal, where each wave
340 corresponds to the record between two successive zero up crossings, that is
341 when the wave-perturbed sea surface moves upward crossing the zero
342 reference level. Then the ensemble average was computed fixing the time
343 (\hat{t}) and arithmetically averaging all the N wave cycles simulated (Eq. 2).
344 Subsequently, the random residual turbulent component of the flow was
345 calculated by subtracting the ensemble phase velocity to the instantaneous
346 velocity (Eq.3). Thus, for regular waves the kinematics could be split into
347 periodic component (mean oscillatory flow) with repetitive vortical
348 structures (LCS), and those related to the turbulent motion.

$$349 \quad \langle \mathbf{u}(x, z, \hat{t})_N \rangle = \frac{1}{N} \sum_{n=1}^N \mathbf{u}_n(x, z, \hat{t}); \quad (2)$$

$$350 \quad \mathbf{u}'(x, z, \hat{t}) = \mathbf{u}(x, z, \hat{t}) - \langle \mathbf{u}(x, z, \hat{t})_N \rangle; \quad (3)$$

351 In order to evaluate the number of wave cycles required to construct the
352 averaged ensemble, convergence tests were performed following the
353 methodological approach in Melville et al. (2002) for the square mean
354 velocity and the turbulent kinetic energy. The tests included all
355 morphological scenarios and wave conditions, and demonstrated that 10
356 wave cycles are enough to guarantee proper separation of steady and
357 turbulent components.

358

359 ***Oscillatory flow characterization.***

360 The mean flow was characterized through the streamwise variation of the
361 horizontal velocity profiles and the bottom boundary layer thickness (δ),
362 defined as the distance from the bottom to the height of maximum
363 horizontal velocity $\langle U_{mo} \rangle$ at the wave phase 90° (Jensen et al., 1989). As
364 well as the oscillatory Reynolds number defined as $Re = aU_{mo} / \nu$, where
365 $\langle U_{mo} \rangle$ the maximum value of the free stream velocity, ν the kinematic
366 viscosity (Jensen et al., 1989), $a = U_{mo}T/2\pi$ is the amplitude of the free
367 stream motion where T is the wave period.

368 ***Large coherent structures***

369 LCS are defined as connected, large-scale turbulent fluid parcels with
370 phase-correlated vorticity over their spatial extent. These are a
371 characteristic feature of turbulent shear flows, and are responsible for the
372 large-scale transport of mass, heat and momentum (Hussain, 1983).
373 Although several mechanisms can induce LCS, we are interested in the
374 horseshoe vortex, the lee-wake vortex, and vortex shedding, which are
375 strongly related to the presence of an obstacle in a flow. Vortex dynamics
376 contribute to the scouring process since bed shear increases under the
377 vortexing.

378 The LCS can be separated from the background flow field through the use of
379 an approximated criterion based on the Okubo-Weiss parameter W:

380 $W = S_n^2 + S_s^2 - \omega^2$ (6), $S_n = d\langle u \rangle/dx - d\langle w \rangle/dz$; (7)

381 $S_s = d\langle w \rangle/dx + d\langle wu \rangle/dz$ (8), $\omega = d\langle w \rangle/dx - d\langle u \rangle/dz$; (9)

382 where S_n is the normal strain, S_s is the shear strain, ω is the vorticity, $\langle u \rangle$ is
383 the ensemble averaged horizontal velocity, and $\langle w \rangle$ is the ensemble
384 averaged vertical velocity.

385 The velocity field can be partitioned into three regions according to the
386 magnitude of this criterion. Rotation dominates regions with $W < -W_0$,
387 where the vortices are located. Intermediate regions are characterized by
388 small positive and negative values of W ($|W| \leq W_0$) where the vorticity and
389 strain rate are balanced. The strain dominated regions, with $W > W_0$, are
390 located outside the vortices. The threshold value is $W_0 = 0.2 \sigma_w$, where σ_w is
391 the standard deviation of W in the analyzed domain (Pasquero et al., 2001).
392 The application of this criterion depicts the general structure of the vortex,
393 with an eddy core in a vorticity-dominated inner region, and a circulation
394 cell in the strain-dominated outer region (Elhmaïdi et al., 1993). The core
395 edge is identified by the closed lines with $W=0$. The W parameter sign for
396 the extraction of eddy cores has been successfully employed in complex
397 fluid flows (Jeong and Hussain, 1995), oceanography (Isern-Fontanet, 2004)
398 and oscillatory flow analysis (Mattioli et al., 2013).

399 The values of the dimensionless vorticity (ω^* ; computed as $\omega^* = \omega T$) and
400 dimensionless Okubo-Weiss parameter (W^* ; computed as $W^* = WT^2$) are
401 calculated from the ensemble averaged velocities.

402 ***Turbulence***

403 The streamwise variation in the vertical distribution of Reynolds stresses
404 ($-\rho \overline{u'w'}$) was computed under different wave conditions (shoaling
405 progressive waves and breaking waves). The results are analysed with
406 streamwise distribution of bed shear stress and mean flow characteristics.

407 **Steady current generated by nonlinear effects induced by waves**

408 **(SCw): Undertow and steady streaming**

409 The steady current, generated by nonlinear effects induced by waves,
410 includes steady streaming and undertow. This wave-induced steady current
411 is estimated by averaging the time series of velocity components in each
412 grid cell over 10 wave periods after the steady state was reached in each
413 simulation.

414 **Bed shear stress**

415 Bed shear stress and friction velocity are fundamental variables in sediment
416 transport and scour investigations. Several criteria are employed to
417 determine the initiation of motion, among them the Shields threshold
418 parameter (Shields, 1936) and the so-called wave mobility number
419 (Nielsen, 1992), which can be used to calculate the critical bed shear stress
420 as a function of sediment characteristics. Analysis of spatial variation of bed
421 shear stress, and the mechanisms involved in its increment around the
422 wreck, was conducted. Bed shear stress for the wave conditions and
423 bathymetric profiles was calculated as $\tau = \nu du/dz$, where dz is the size of the
424 first grid cell ($\sim 0.005\text{m}$).

425 The threshold Shields parameter was calculated according to Soulsby
426 (1997).

427
$$\theta_{cr} = \frac{0.3}{1+1.2D_*} + 0.055[1 - \exp(-0.02D_*)]; \quad D_* = d \left[\frac{g(\rho_s - \rho)}{\nu^2} \right]^{1/3}; (10)$$

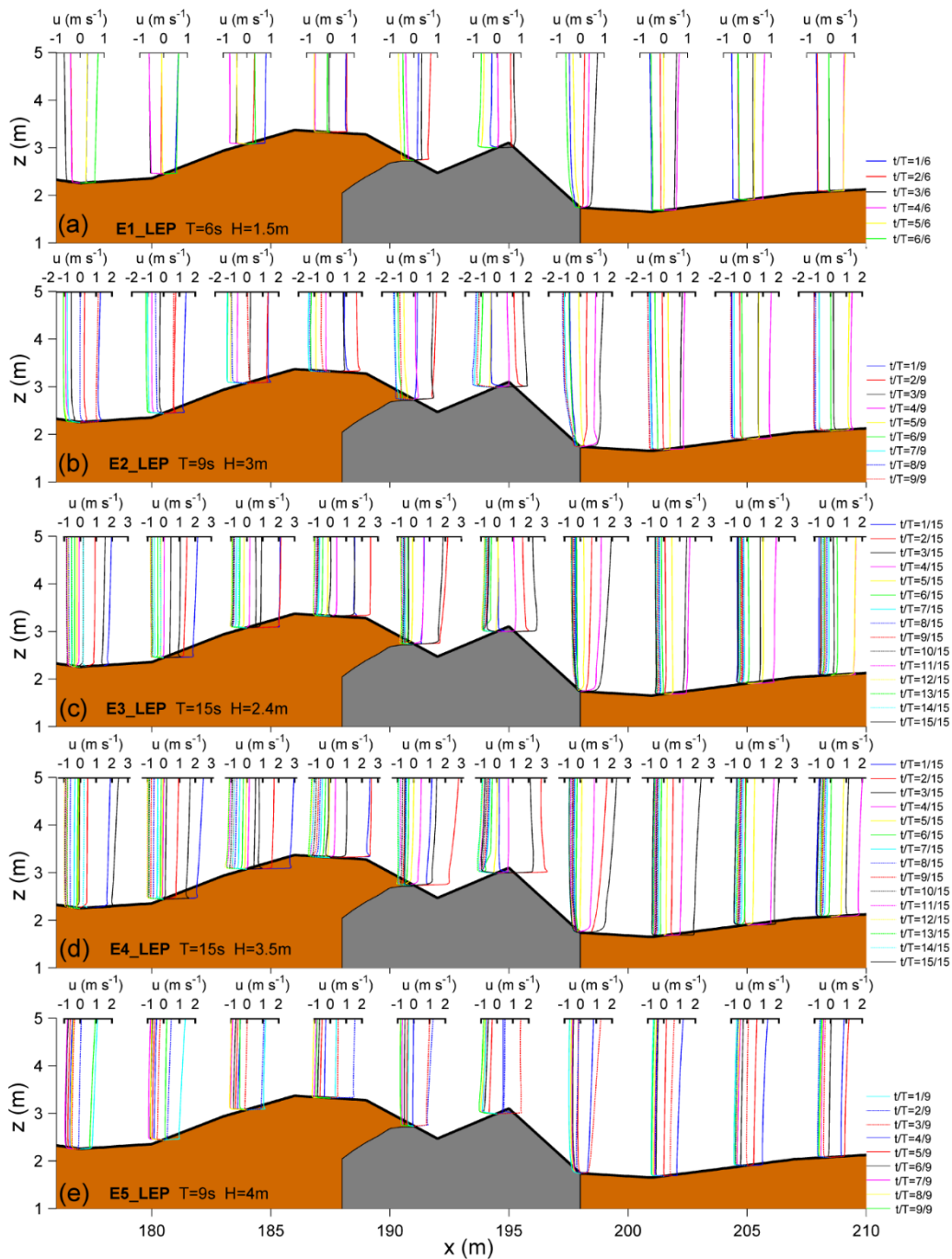
428 where D_* is the dimensionless grain size, d is the grain diameter, ν is the
429 kinematic viscosity and ρ_s is the sediment grain density assumed as quartz
430 density.

431 The critical bed shear stress follows from the definition of the Shields
432 parameter $\tau_{cr} = dg(\rho_s - \rho)\theta_{cr}$ and is modified for a sloping seabed according
433 to the expressions for downslope flow $\tau_c = \tau_{cr}[\sin(\phi_i - \beta) / \sin \phi_i]$ and upslope
434 flow $\tau_c = \tau_{cr}[\sin(\phi_i + \beta) / \sin \phi_i]$, where β is the bed slope and ϕ_i the angle of
435 repose of the sediment ($\phi_i = 32^\circ$ according to Soulsby (1997)).

436 **4 Results**

437 **4.2 Oscillatory flow characterization**

438 Figure 3 depicts the vertical distribution of horizontal velocity from the
439 numerical experiment conducted using LEP bathymetry. Velocity profiles
440 correspond to different wave phases as a function of t^* , being $t^* = t/T$. Near
441 bottom velocities around the wreck are increased in the first few
442 centimetres above the seabed. The wreck remains act as a splitter, where
443 the velocity amplification produces fluid separation. As the wave height and
444 period increases, flow velocity increases (Figure 3a and Figure 3d). The
445 difference between the upwave ($x=191$) and downwave ($x=198$ m) velocity
446 profiles are notable. The depth reduction at the offshore ($x < 190$) sediment
447 accumulation increases near bottom orbital velocity, whereas inshore it was
448 reduced ($x < 200$ m). The differences between upwave and downwave areas
449 become more evident with the increase in wave height and period. Wave
450 asymmetry increases as function of H and T , especially for larger periods
451 (Figure 3b and Figure 3c). The unperturbed horizontal velocity profile was
452 altered in the nearness of the shipwreck ($x=190-200$ m). It is observed
453 upwave and downwave of the wreck (see for example Figure 3b at $t^* = 6/9$
454 and $7/9$ and downwave ($x=198$) at $t^*=2/9$ and $t^*=4/9$).

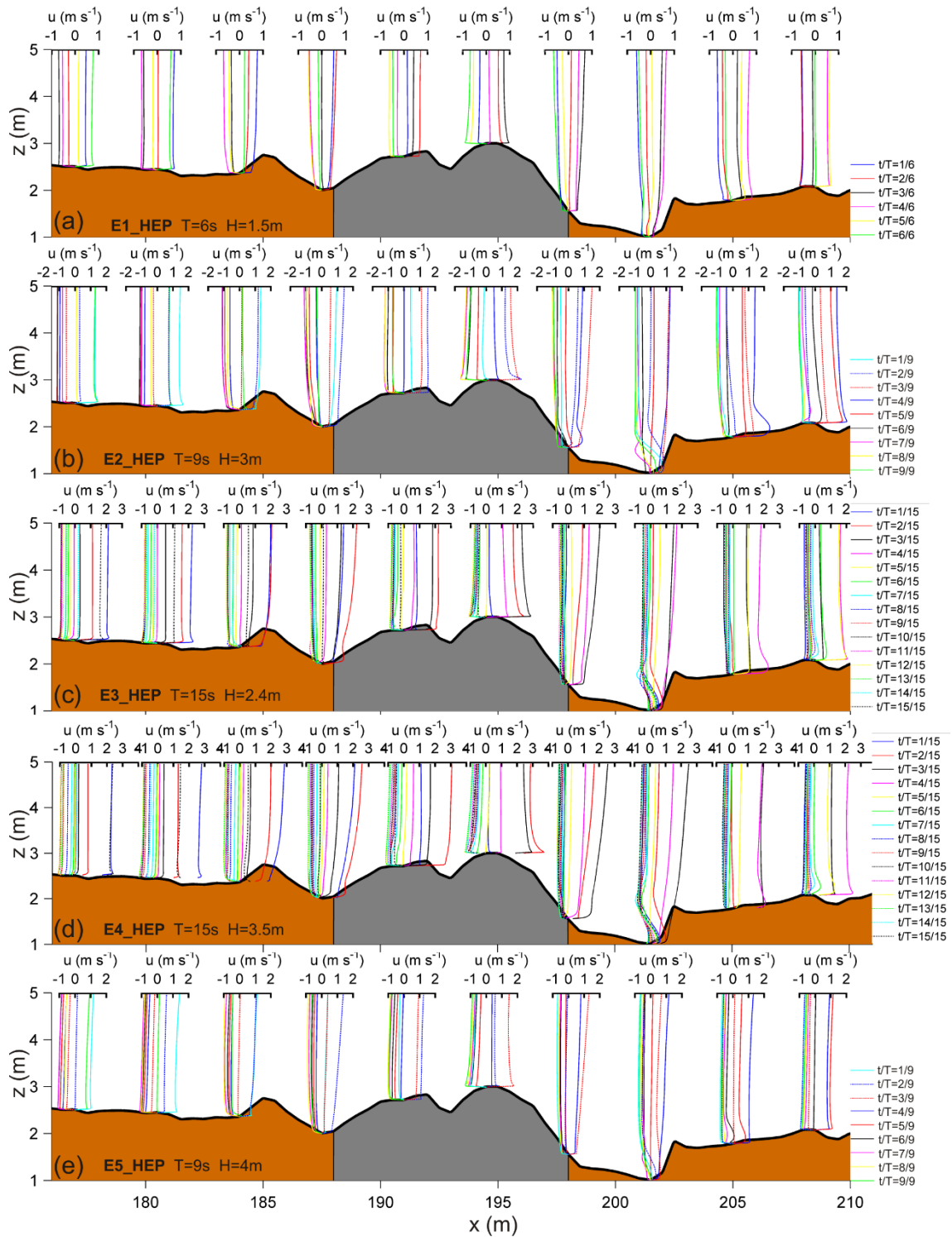


455

456 Figure 3. Vertical distribution of horizontal velocity at different streamwise locations
 457 for LEP bathymetry. Information relative to the wave phase variation is represented
 458 as a function of the t^* ratio for the different line colours and line styles. The grey
 459 colour marks the location of the hull remains.

460 Figure 4 shows the vertical distribution of horizontal velocity for the
 461 numerical experiment conducted with the HEP bathymetry. The perturbed

462 velocity profiles extend further than in the case of LEP ($x=184\text{m}$ and
463 $x=205\text{m}$), especially downwave of the wreck. A relative increase in
464 maximum near bed velocity is noted with respect to LEP conditions($x=191\text{m}$
465 and $x=194.5\text{ m}$) (Figure 4a to Figure 4d). Wave height increase and longer
466 periods expand this phenomenon up to the toe of the wreck ($x=198$)
467 (Figure 4d). Despite of depth increase, the inshore scour pit does not
468 produce a notable reduction of near bottom velocity ($x=201.5$). HEP
469 upwave and downwave dissimilarities are larger than under LEP conditions,
470 with the exception of the offshore wave breaking (Figure 4e). Amplification
471 of wave asymmetry with the increased H and T is larger than with LEP at
472 the hull remains (see for example Figure 4b and Figure 4c). The shape of
473 the velocity profiles is markedly modified at the toe of wreck ($x=198\text{m}$)
474 (Figure 4b ($t^*=4/9$ to $t^*=7/9$)), and at the deepest scour pit ($x=201.5$)
475 (Figure 4b ($t^*=1/9, 2/9, 7/9, 8/9, 9/9$)).



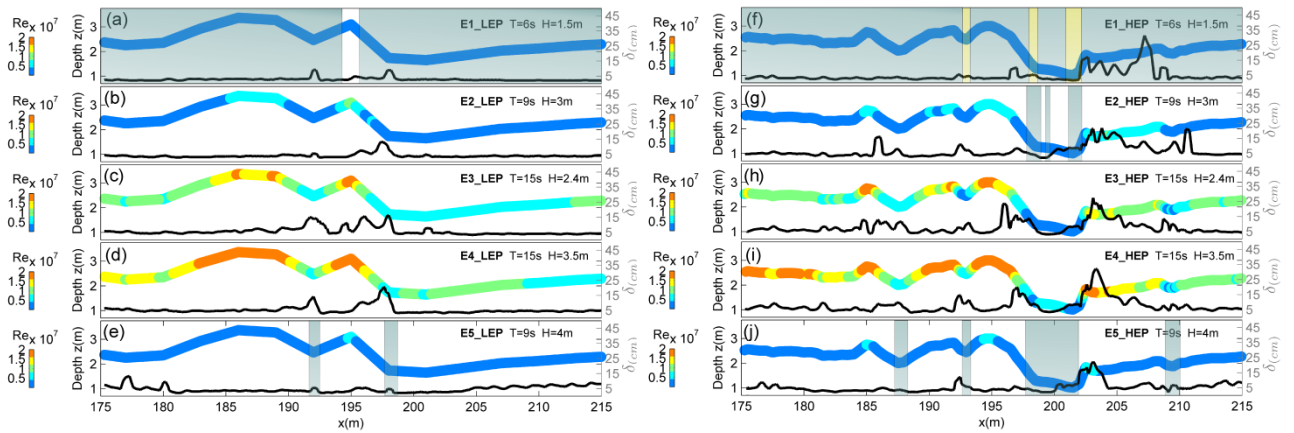
476

477 Figure 4. Vertical distribution of horizontal velocity at different streamwise locations
 478 for HEP bathymetry. Information relative to the wave phase variation is
 479 represented as a function of the t^* ratio for the different line colours and line styles.

480 Figure 5 shows the wave Reynolds number (Re) (colour scaled) and
481 boundary layer thickness (δ) (black line), under LEP (left panel) and HEP
482 (right panel) conditions. The LEP simulations are dominated by fully
483 turbulent flow, with the exception of the transitional regime observed in
484 E1_LEP (Figure 5a). The wave Reynolds number follows a similar spatial
485 variation in all LEP experiments; amplification over the top of the wreck
486 ($x=194.5$) and at the offshore sand accumulation (Figure 5b, Figure 5d).
487 The boundary layer thickness increases from 3.5 cm in E1_LEP (Figure 5a)
488 to nearly 7 cm in E4_LEP (Figure 5d). Two peaks are identified at the wreck
489 ($x=192.4$ m) and at the toe of wreck remains ($x=197$ m). In addition, in all
490 experiments δ increases over the wreck, reaching a maximum between 5
491 cm (Figure 5a) and 20 cm (Figure 5d) at $x\sim 196$ m, which is probably
492 associated with the flow separation point. In the E3_LEP simulation (Figure
493 5c), a maximum is observed upwave of the wreck. In E5_LEP a progressive
494 increase of δ in the downwave region.

495 The HEP simulations (right panels) also show the predominance of turbulent
496 flow. However, laminar flow at the wreck is observed in E1_HEP (Figure 5f),
497 and a transitional regime in the inshore scour pits and in the offshore scour
498 pits in E2_HEP (Figure 5g). Likewise, a transitional regime was observed at
499 the centre of the wreck site and downwave of the wreck ($x\sim 210$) in
500 E5_HEP. The Re increases over the wreck and in the offshore scour crest,
501 decreasing at the inshore and offshore scour pits. The boundary layer
502 thickness shows values slightly higher than those found for LEP experiments
503 and new peaks associated with the offshore scour crest feature ($x\sim 185$).
504 However, the larger differences appear downwave of the wreck, at the
505 deepest area of the inshore scour pits ($x\sim 200$) and especially beyond the

506 inshore scour pit, where peaks (15 cm-30 cm) are noted (Figure 5f to
 507 Figure 5j).

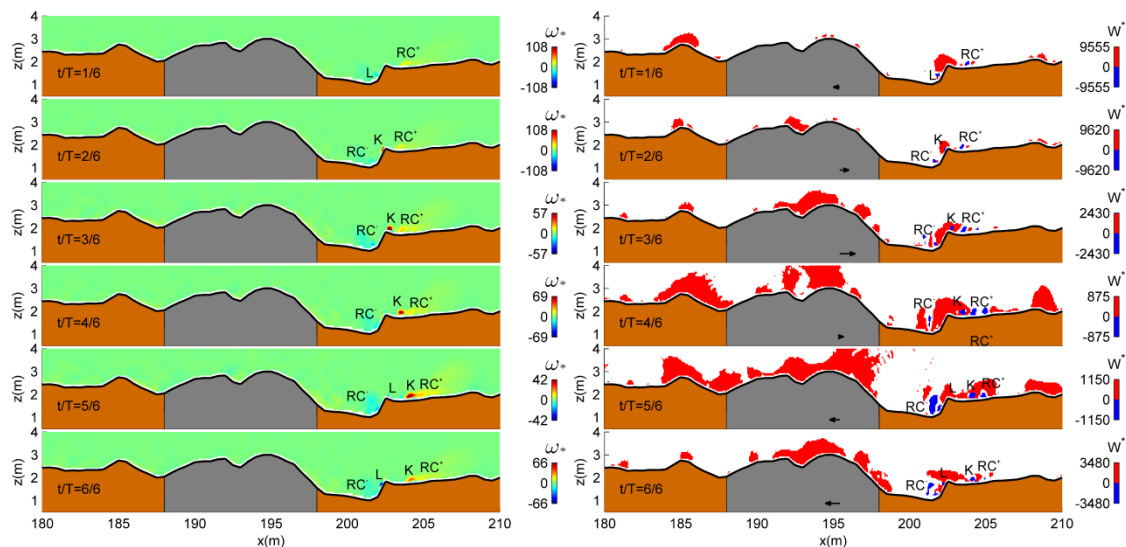


508
 509 Figure 5. Wave Reynolds number (Re) colour scale stamped on bathymetry profile
 510 (depth left axis) and boundary layer thickness (δ) black line (right axis). Left panel
 511 shows numerical experiments for LEP conditions. Right panel shows numerical
 512 experiment for HEP conditions. The yellow overlay indicates laminar regime
 513 ($Re < 1.5 \cdot 10^5$), the grey overlay marks a transitional regime ($1.5 \times 10^5 < Re < 10^6$), and
 514 no colour overlay indicate fully turbulent flow ($Re > 10^6$).

515 4.3 Large coherent structures

516 The evolution during the wave phase (as a function of $t^* = t/T$) of
 517 dimensionless vorticity (ω^*) is shown in the left panels, and the
 518 corresponding values of the dimensionless Okubo-Weiss parameter (W^*) are
 519 shown in the right panels in Figures 6-10. In the case of ω^* , the cold colour
 520 represents negative vorticity and warm colour represents positive vorticity.
 521 In the case of W^* , the red colour indicates strain dominated areas, the blue
 522 colour shows areas dominated by vorticity, and white indicates areas
 523 characterized by small positive and negative values of W ($|W| \leq W_0$) where
 524 the vorticity and strain rate are balanced. Vectors located at position ($x=1$,
 525 $Z=195$) in the right panels show the sequence of horizontal velocity

526 registered at 4 m depth at $x=194.5$. It should be noted that variable colour
 527 scales are used to highlight the different LCS.



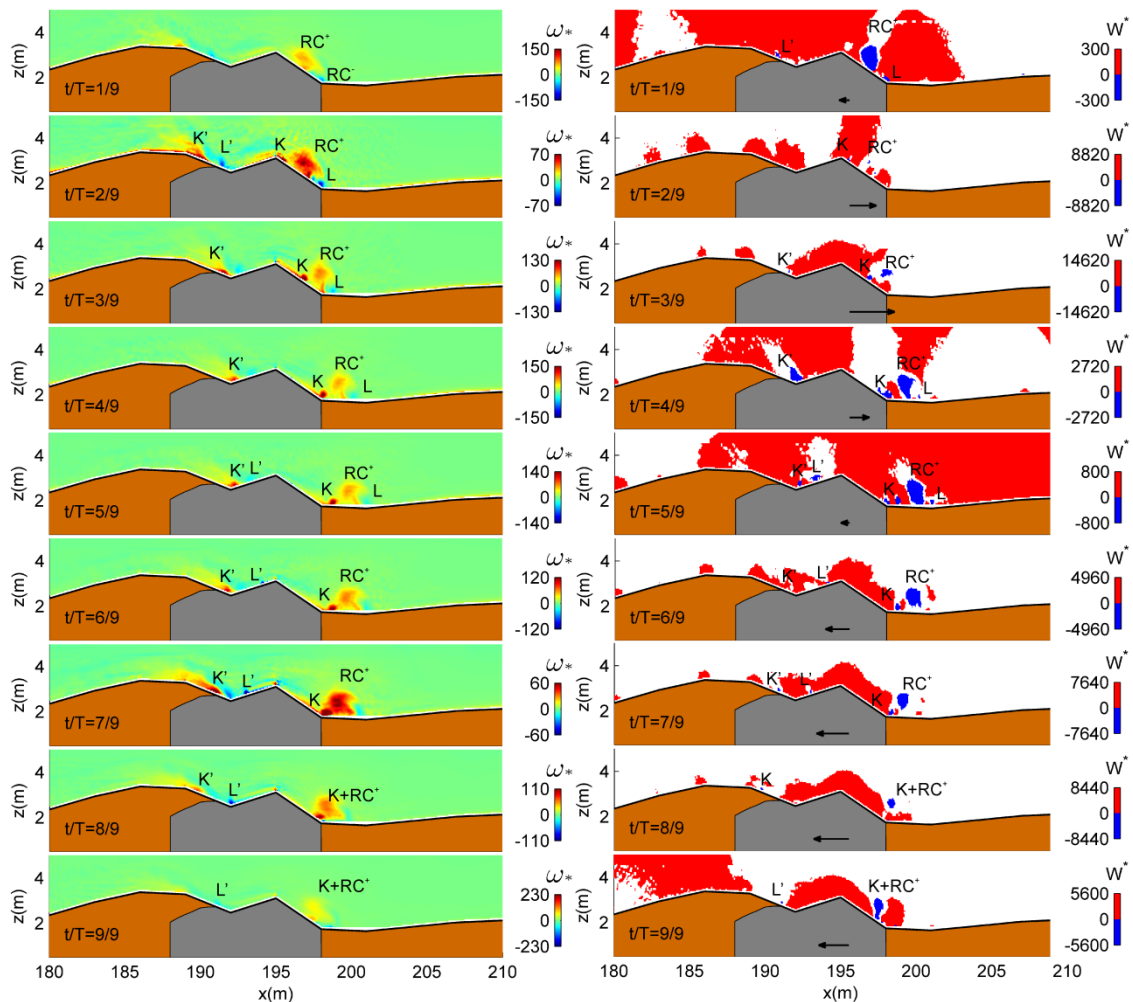
528

529 Figure 6. Temporal sequence of dimensionless vorticity (left) and the dimensionless
 530 Okubo-Weiss parameter (right) for a mean wave cycle in the E1_HEP experiment.
 531 Vectors show the horizontal velocity at 4 m depth at $x=194.5$.

532 The E1_LEP simulation (not illustrated) does not present relevant vortical
 533 structures. On the contrary, in E1_HEP (Figure 6), a vortex K located at the
 534 inshore scour-crest system is flipped over the inshore scour crest ($t^*=2/3$)
 535 moving shoreward during positive flow acceleration. At the leeside of the
 536 inshore scour crest a negative vorticity structure (L) is generated at
 537 ($t^*=5/6$) flipping over the scour crest during the streamwise negative
 538 velocity phase ($t^*=6/6$). A permanent positive vorticity structure (RC^+) is
 539 located downwave and RC^- is found at the inshore scour pits and is present
 540 during all wave phases.

541 In simulation E2_LEP (Figure 7) a counterclockwise rotation vortex (positive
 542 vorticity) originates upwave and flips over the wreck ($t^*=2/6$) to reach the
 543 toe of hull remains at $t^*=4/9$. On the offshore side, a small K' vortex ($\omega^* >$

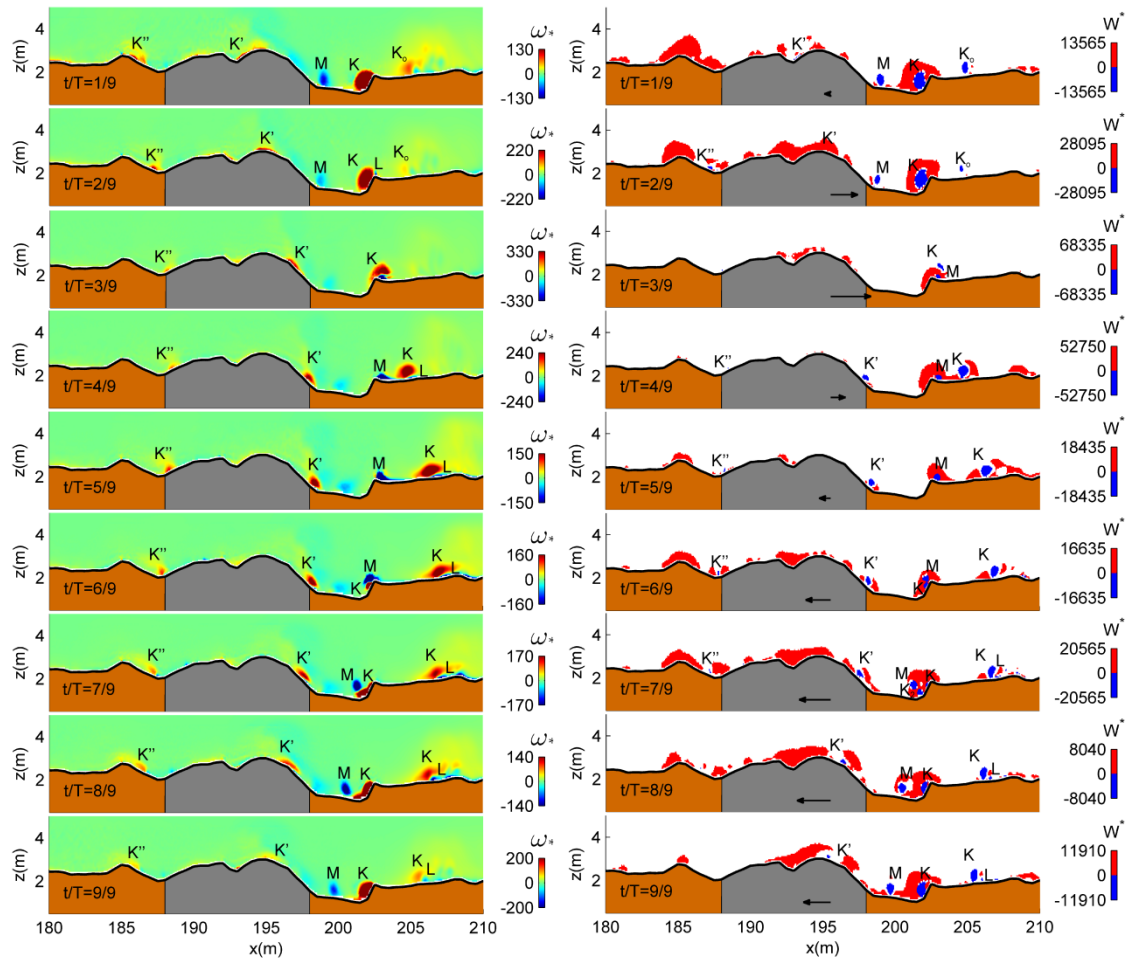
544 0) formed above the sediment accumulation moves towards the wreck ($t^*=$
 545 $2/9 - 5/9$) with shoreward flow and in the opposite direction ($t^*=6/9-8/9$).
 546 Another small vortex L' ($\omega^* < 0$) produced upwave of the wreck ($t^*=2/9$)
 547 moves around the hull ($t^*=5/9 - 9/9$). A small eddy L with negative vorticity
 548 generated ($t^*=2/9$) at the toe of the wreck is dragged shoreward during the
 549 positive horizontal velocity phase ($t^*=4/9-5/9$). In addition, the location of
 550 a larger counter-clockwise rotation structure (RC^+) oscillates upwave-
 551 downwave with the horizontal velocity throughout the whole wave cycle.



552
 553 Figure 7. Temporal sequence of dimensionless vorticity (left) and the dimensionless
 554 Okubo-Weiss parameter (right) for a mean wave cycle in the E2_LEP experiment.
 555 Vectors show the variation of horizontal velocity at 4 m depth at $x=194.5$.

556 The results corresponding to the simulation E2_HEP are shown in Figure 8.
557 An eddy with positive vorticity K' generated in the previous wave cycle over
558 the wreck ($x=193$) is washed over the hull remains when the wave
559 propagates and it reaches the toe of the wreck ($t^*=4/9-5/9$) (right panels
560 Figure 8). Subsequently, during the negative horizontal velocity phase, K' is
561 carried seawards over the wreck from $t^* =5/9$ to $t^* =9/9$, similar to
562 E2_LEP. The flow acceleration produces elongation of the vortex in the
563 horizontal direction.

564 At the inshore scour pit, a larger K vortex with counterclockwise rotation is
565 observed at $t^*=1/9$, along with the vortex (K_0) developed during the
566 previous wave cycle. K is generated by seaward flow($t^*=6/9$). It flips over
567 the inshore scour crest during a positive horizontal velocity phase, and
568 forms a paired vortex with a small clockwise vortex (L) formed at the top of
569 scour crest ($t^*=2/9$). They subsequently shed, moving seaward ($t^*=2/9-$
570 $t^*=5/9$) as is shown by the vorticity field. At the moment of maximum
571 positive velocity ($t^*=3/9$), after the flow acceleration phase, a new
572 clockwise vortex (M) arises at the lee side of the scour crest ($x=202.5$). The
573 M vortex initially forms a vortex pair with K_2 and it is washed seaward as far
574 as the toe of the wreck. At the offshore scour pit, a small vortex K'' ($\omega^* > 0$)
575 is observed trapped between $x=186$ and $x=188$.



576

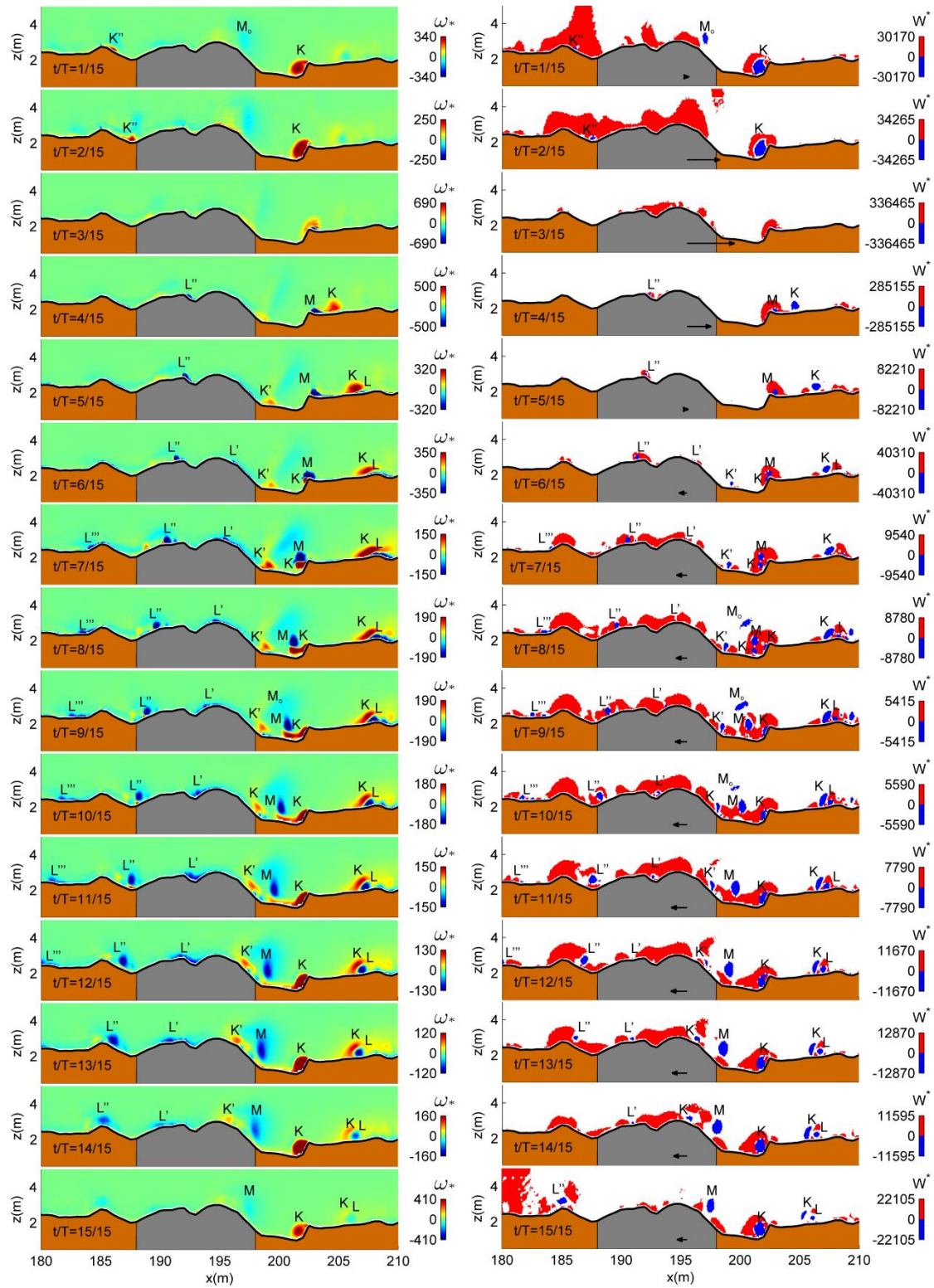
577 Figure 8. Temporal sequence of dimensionless vorticity (left) and the dimensionless
 578 Okubo-Weiss parameter (right) for a mean wave cycle in the E2_HEP experiment.
 579 Vector show the variation of horizontal velocity at 4 m depth at $x=194.5$

580 The vortex dynamics corresponding to simulation E3_LEP (not shown) is
 581 similar to E2_LEP without the development of the RC⁺ and L.

582 In the E3_HEP (Figure 9) vortex dynamics is similar to that of E2_HEP at
 583 the inshore scour-crest. However, unlike E2_HEP, the M vortex crosses the
 584 inshore scour pits detached from the seabed, and rises when it reaches the
 585 wreck. Subsequently, at the beginning of the wave cycle ($t^*=1/15$), M_0 (the
 586 vortex M in the previous wave cycle) is transported shoreward (left panel at
 587 $t^*=7/15$, and right panel at $t^*=8/15$). On the other hand, it should be

588 noted that the large L' vortex ($\omega^* < 0$) generated downwave of the wreck
589 during the positive horizontal velocity phase, flips over the wreck ($t^*=6/15-$
590 $14/15$). Also, a L'' vortex (negative vorticity) located upwave of hull remains
591 originates at the the wreck site ($x=192.7\text{m}$) at $t^*=4/15$ and is transported
592 by the mean flow seaward to the offshore scour crest ($t^*=5/15-5/15$).

593 At the offshore scour-crest system, the K'' vortex is identified only at
594 $t^*=1/15-2/15$ at the leeside of scour-crest. Likewise, a vortex L''' is also
595 captured when it flips over the scour-crest ($t^*=7/15-12/15$).



596

597 Figure 9. Temporal sequence of dimensionless vorticity (left) and the dimensionless

598 Okubo-Weiss parameter (right) for a mean wave cycle in the E3_HEP experiment.

599 Vector show the variation of horizontal velocity at 4 m depth at x=194.5

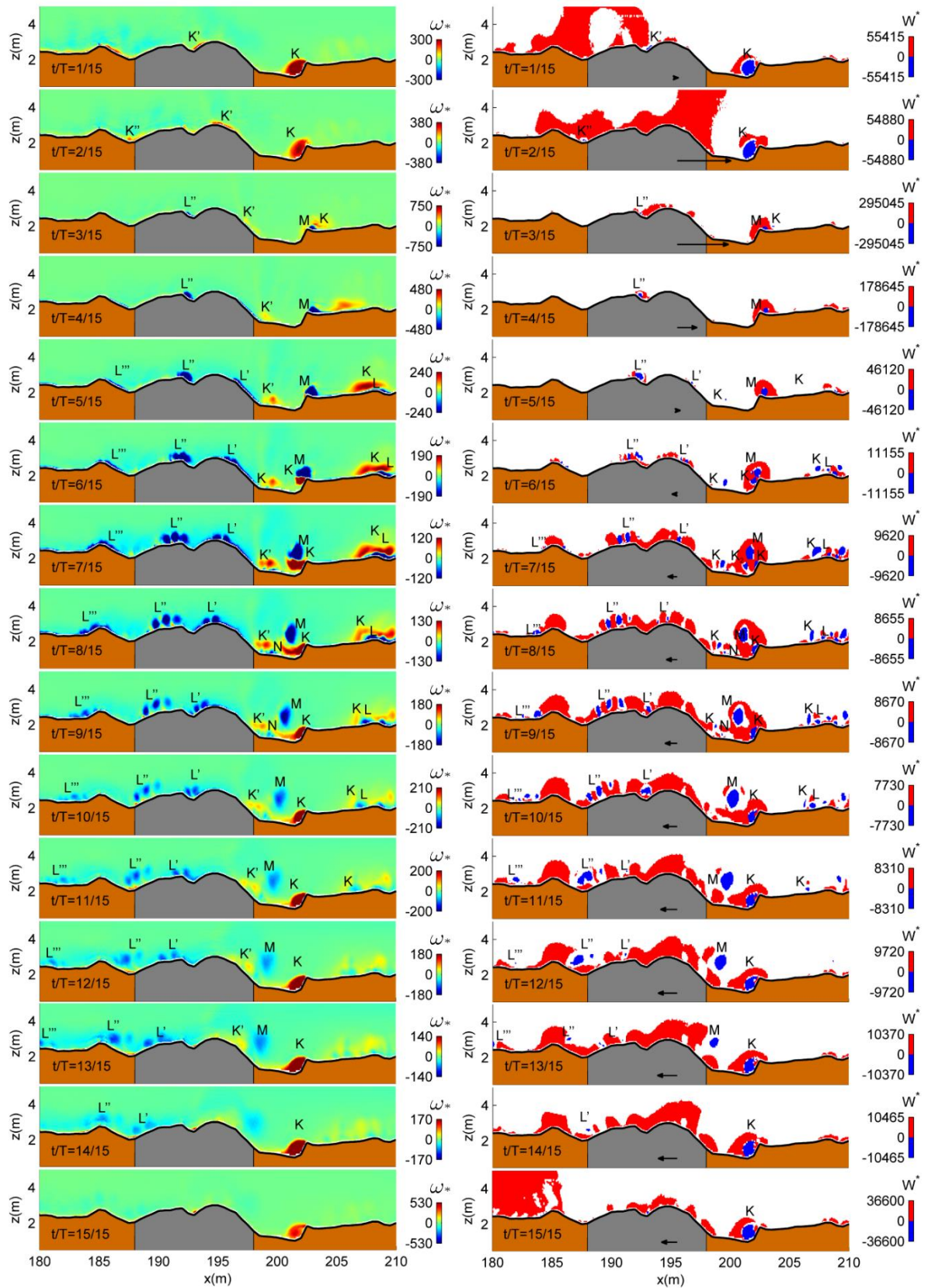
600 E4_LEP vorticity pattern resembles that of E3_LEP, although some
601 differences appear. The eddy with counterclockwise rotation at the toe of
602 the wreck is horizontally elongated, and is eventually split into two vortices
603 ($t^*=6/15$) by the mean flow. Additionally, there is an increase in size in the
604 clockwise vortex at the centre of the wreck site ($t^*=10/15$). The L'' vortex
605 generated at the centre of the wreck site during the deceleration phase of
606 shoreward flow is strained over the sediment accumulation ($x=185$) during
607 the seaward flow phase.

608 The system of coherent structures developed in simulation E4_HEP (Figure
609 10) shows higher complexity than in the other cases. At the inshore scour-
610 crest system, the process of vortex formation and shedding is similar to the
611 E3_HEP experiment. A larger K-type vortex of 1.2 m diameter is located at
612 the inshore scour mark, and an M vortex is generated after the maximum
613 positive velocity downwave of scour crest. In this case, an L and K vortex
614 pair emerge ($t^*=5/15$) at $x\sim 208$. Additionally, a system of small vortices is
615 present at $x=208-210$.

616 In the inshore scour pits the K vortex ($t^*=7/15$) is also divided generating a
617 K_2 vortex. The negative vorticity eddy M created downwave of the inshore
618 scour ridge ($x=202$) at $t^*=3/15$, is larger in size (1.10 m diameter) and it
619 follows a seaward trajectory detached from the seabed.

620 At the wreck, the vortex formation process is better developed than in
621 previous simulation and is accompanied by a new clockwise eddy N
622 ($t^*=7/15-9/15$). The L' vortex splits into smaller vortices as the seaward
623 flow washes over the hull structure ($t^*=7/15-9/15$). Likewise, the L'' vortex
624 formed in the centre of the wreck site divides into smaller eddies.

625 At the offshore scour crest a similar process takes place, where vortex L'''
626 flips over the offshore crest and divides into smaller structures during the
627 negative velocity phase ($t^*=10/15$).



628

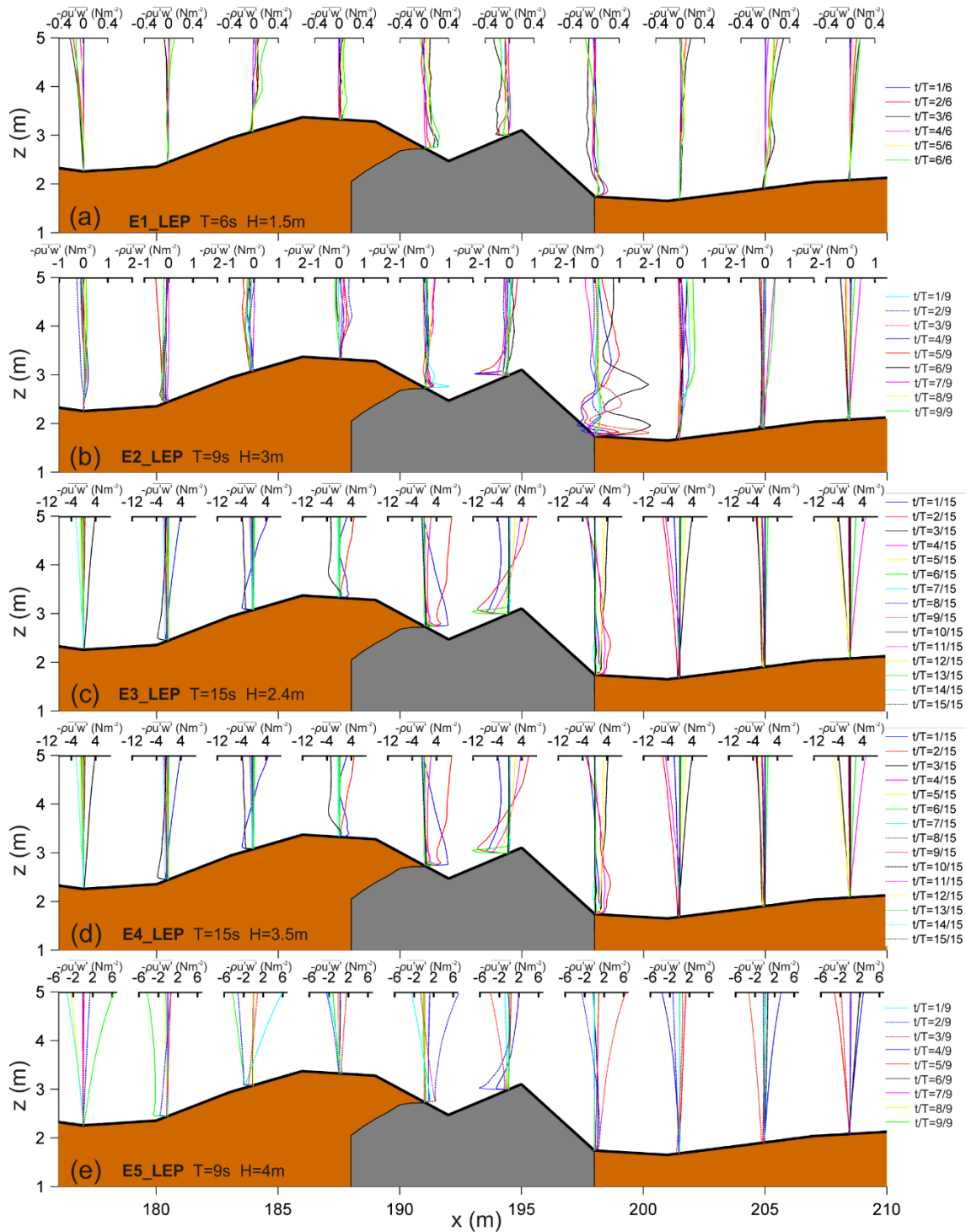
629 Figure 10. Temporal sequence of dimensionless vorticity (left) and the
 630 dimensionless Okubo-Weiss parameter (right) for a mean wave cycle in the E4_HEP

631 experiment. Vector show the variation of horizontal velocity at 4 m depth at
632 $x=194.5$

633 Simulation E5_LEP (not shown) is similar to E2_LEP. In E5_HEP, vortices
634 are only identified in the inshore and offshore scour-crest systems. At the
635 inshore, the two vortex pairs upwave and downwave of the scour crest are
636 observed simultaneously, remaining on or near the scour crest, unlike in
637 previous HEP simulations. Also, the L vortex of the K-L pair downwave of
638 the scour crest grows in size ($t^*=7/9-8-9$).

639 **4.4 Turbulence**

640 Figure 11 shows the vertical distribution of turbulent shear stress from
641 simulations using LEP bathymetry with maximum values located around the
642 wreck ($x=190-200$). Shear stress profiles located at the offshore sediment
643 accumulation show a higher level of turbulence near bed in E3_LEP (Figure
644 11c), E4_LEP (Figure 11d) and E5_LEP (Figure 11e). In the case of E4_LEP,
645 after the wave breaking point ($x=200$) no increment of turbulent shear
646 stress at the seabed is observed. However, in E5_LEP (wave breaking point
647 at $x=89$) higher levels of turbulence are observed on the offshore side of
648 the wreck.



649

650 Figure 11. Vertical distribution of residual horizontal turbulent shear stress

651 ($-\rho \overline{u'w'}$) at different streamwise locations simulated with the LEP

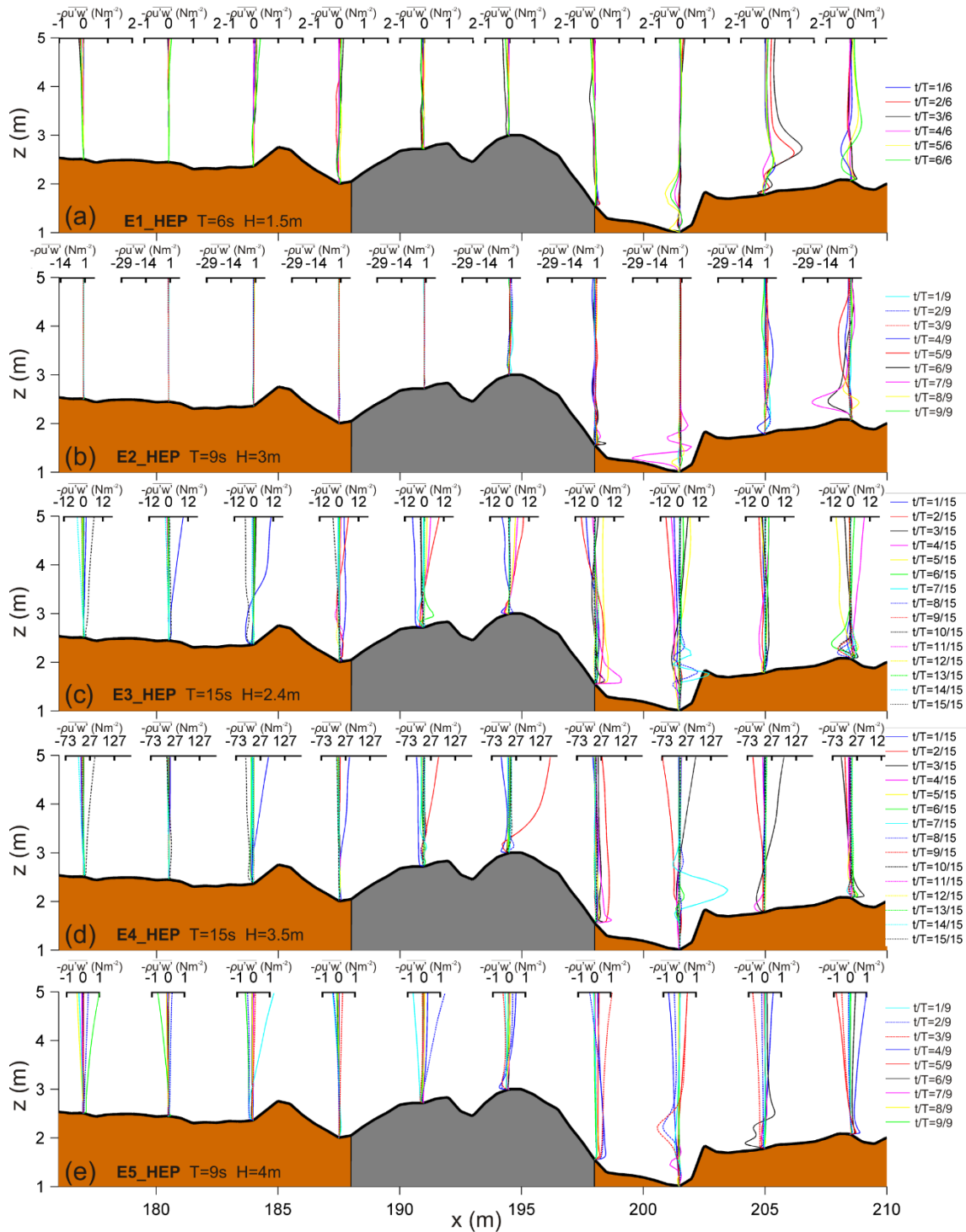
652 bathymetry (note that different scales are used in the experiments to

653 highlight the variation of $-\rho \overline{u'w'}$). Information relative to the wave phase

654 variation is represented as a function of the t^* ratio for the different line
655 colours and styles

656

657 In the case of HEP bathymetry (Figure 12) the areas of maximum shear
658 stress are concentrated downwave of the wreck, in the near bed region.
659 Unlike the LEP simulation, near bed shear stress is reduced upwave of the
660 hull remains with respect to the downwave area. Similar to the LEP
661 simulation, wave breaking introduces higher levels of turbulence into the
662 system as indicated by larger values of shear stress (Figure 12d).



663

664 Figure 12. Vertical distribution of residual horizontal turbulent shear stress ($-\rho \overline{u'w'}$)
 665 at different streamwise locations simulated with the HEP bathymetry (note that
 666 different scales are used in the experiments to highlight the variation of $-\rho \overline{u'w'}$).
 667 Information relative to the wave phase variation is represented as a function of t^*
 668 ratio for the different line colours and line stile.

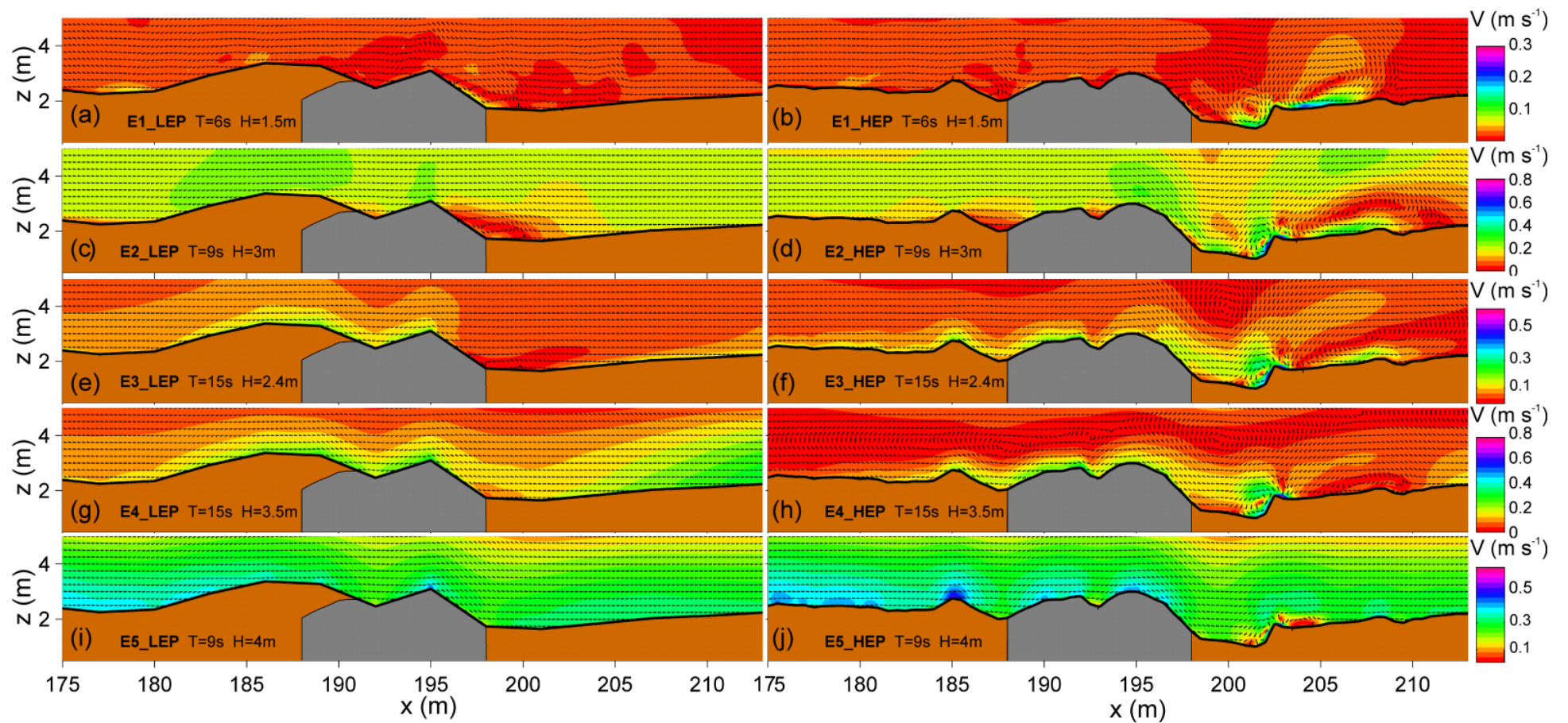
669 **4.5 Steady currents generated by nonlinear effects induced by**
670 **waves (SCw): undertow and steady streaming.**

671 LEP simulations indicate steady currents (Figure 13, left panels) are more
672 intense in the near bed region over the hull remains and the offshore
673 sediment accumulation. The increment in wave height and periods produces
674 SCw intensification (see Figure 13a and Figure 13c). A counterclockwise
675 current cell developed at the toe of the hull ($x \sim 197\text{m}$) and the SCw
676 intensification is observed in the near bottom region in E1_LEP (Figure 13a).
677 In the case of simulation E3_LEP (Figure 13e) the SCw enhancement (< 0.3
678 $\text{m}\cdot\text{s}^{-1}$) is mainly restricted to the near bed region. In E4_LEP, wave breaking
679 produces an increase in SCw ($0.3\text{m}\cdot\text{s}^{-1}$) over the wreck, at the offshore sand
680 accumulation (from $x=180$ to $x=190$) and downwave of the breaking point
681 ($x \sim 200\text{ m}$). Larger SCw values ($0.4\text{ m}\cdot\text{s}^{-1}$), especially upwave of the wreck,
682 are simulated in the offshore wave breaking case (Figure 13i).

683 HEP bathymetry steady currents (right panels of Figure 13) demonstrate a
684 wave-parameter dependence similar to that observed in the LEP bathymetry
685 runs, and SCw intensification above the wreck is again simulated. However,
686 notable differences between the LEP and HEP simulations are also observed.
687 Unlike LEP, in HEP the maxima steady current are located above and
688 downwave of the wreck, with the exception of E5_HEP. In addition, the
689 presence of the recirculation cells increases the magnitude of SCw
690 downwave of the wreck. For the small waves simulation (Figure 13b), a
691 counter clockwise rotation cell forms at the toe of wreck ($\text{}$), a clockwise
692 circulation cell ($0.15\text{ m}\cdot\text{s}^{-1}$) is located in the deepest part of the inshore
693 scour pit, and another counter-clockwise current cell ($x \sim 205\text{m}$) shows a
694 SCw intensity of $0.20\text{ m}\cdot\text{s}^{-1}$ close to the seabed. In the E2_HEP simulation

695 (Figure 13d), the SWc velocity is increased to $0.3 \text{ m}\cdot\text{s}^{-1}$ in the centre of the
696 inshore scour pits, and the clockwise rotation current cell at the inshore
697 scour mark ($x\sim 202\text{m}$) increases velocity up to $0.3\text{-}0.7 \text{ m}\cdot\text{s}^{-1}$. The counter
698 clockwise rotation cell located at $x\sim 207$ reaches up to $0.35 \text{ m}\cdot\text{s}^{-1}$ near the
699 seafloor. In the E3_HEP simulation (Figure 13f) it is notable how the
700 maximum velocity above the wreck extends to the inshore scour pit, and is
701 associated with the larger current cell with clockwise rotation observed
702 above the inshore scour.

703 The breaking process in E4_HEP produces a volume flux in the shoreward
704 direction within water column (see shoreward direction of vector between 4
705 and 5 m depth in Figure 13h), it restricts the undertow current near to the
706 seabed and intensifies the SCw ($0.15 \text{ m}\cdot\text{s}^{-1}\text{-}0.20 \text{ m}\cdot\text{s}^{-1}$) around the wreck.
707 In addition, a new current cell develops above the offshore scour pits
708 ($x\sim 188$), and weakens the horizontally elongated current cell ($x\sim 207$).



709

710 Figure 13. Steady current generated by nonlinear effects induced by waves. Left panel shows numerical experiments for LEP conditions.

711 Right panel shows numerical experiment for HEP conditions. Cold colours indicate higher velocities and warm colours indicate lower

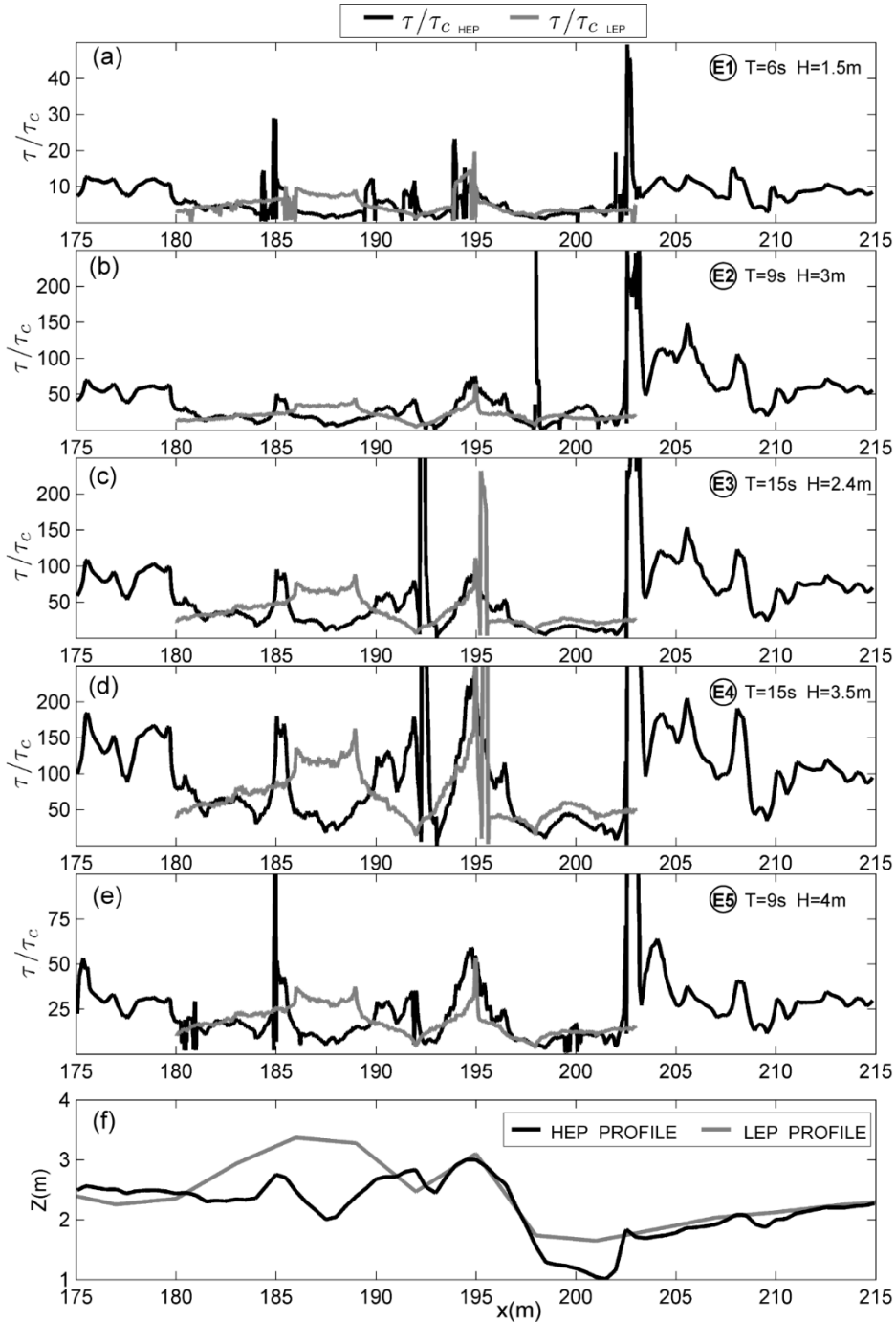
712 velocities.

713 In the E5_HEP simulation, the offshore breaking wave increases SCw
714 current velocity to $0.3 \text{ m}\cdot\text{s}^{-1}$, while the inshore current cell reduces in size
715 and velocity (Figure 13j).

716 **4.6 Bed shear stress**

717 Live-bed scouring dominates the entire site since the bed shear stress is
718 larger than critical bed shear stress for sediment motion in all wave
719 conditions tested. Figure 14 (a-e) depicts the spatial distribution of the ratio
720 between bed shear stress (τ) and critical bed shear stress for the sloping
721 bed (τ_c), with the bathymetric profiles corresponding to HEP and LEP plotted
722 below (Figure 14f). Note that different scales used for ease of interpretation
723 of the τ/τ_c features. For all simulations, larger values of τ/τ_c are obtained at
724 and downwave from the wreck. The maximum τ/τ_c occurs downwave of the
725 wreck ($x\sim 200\text{m}$), it is more evident in the HEP simulations. The τ/τ_c
726 variations induced by bathymetric changes are clear in the larger values of
727 τ/τ_c in the LEP simulations at the sand accumulation upwave of the wreck
728 ($x=185\text{m}-190\text{m}$). In addition, the LEP τ/τ_c maximum occurs around $x=195$
729 at the top of the wreck (Figure 14f), where after a gradual increase the bed
730 shear stress peaks before flow separation. In the HEP simulations
731 bathymetric peaks of τ/τ_c occur on the offshore scour crest ($x=185\text{m}$), near
732 the centre of the wreck site ($x\sim 192\text{m}$), just downwave of the top of the
733 wreck ($x\sim 194.5\text{m}$), and at the inshore scour crest ($x\sim 202.5\text{m}$). Notable
734 also are maxima of τ/τ_c beyond the inshore scour crest ($x=203\text{m}-210\text{m}$).
735 The increase in wave height and period increases the τ/τ_c ratio significantly.
736 Figure 14d shows the τ/τ_c maximum values for longer and higher waves just
737 before breaking ($x=205$), and corresponding to the maximum differences

738 between LEP and HEP experiments. Finally, for simulations E5_LEP and
 739 E5_HEP (Figure 14e), τ/τ_c is reduced due to the drastic reduction of wave
 740 height caused by the offshore wave breaking ($x=89\text{m}$).



741

742 Figure 14. Spatial distribution of the ratios between bed shear stress calculated and
 743 critical bed shear stress for the sloping bed for the two morphological statuses
 744 analyzed. (a) Experiments E1_HEP and E1_LEP. (b) Experiments E2_HEP and

745 E2_LEP. (c) Experiments E3_HEP and E3_LEP. (d) Experiments E4_HEP and
746 E4_LEP. (e) Experiments E5_HEP E5_LEP. (f) Bathymetric profiles corresponding to
747 HEP and LEP.

748 **5 Discussion**

749 Wreck-wave interaction and its seasonal variation was analyzed using
750 computational fluid dynamic simulations at the *Fougueux* site. This method
751 allowed us to evaluate the relative importance of the different processes
752 involved in scouring at a fully-submerged, wave-dominated historic
753 shipwreck site, under the influence of seasonal forcing. Our analysis reveals
754 characteristics of the mean oscillatory flow, flow velocity increase,
755 coherency of structures, recirculation cells and residual turbulence.

756 Although the two bathymetric profiles (LEP and HEP) used in the study were
757 obtained from different sources (multibeam and single beam) and are of
758 different resolution, the variations introduced in the shipwreck shape
759 representation are minor in comparison to the flow pattern variations
760 induced by morphological changes (Figure 1c).

761 The analysis of oscillatory flow for the different wave conditions reveals that
762 seasonal morphological changes largely modify the oscillatory flow velocity
763 pattern around the shipwreck. The inshore and offshore scour observed in
764 HEP simulations promotes the reduction of maximum and minimum near
765 bottom velocity values as a direct consequence of depth increase in both
766 areas (Figures 3 and 4). These modifications occur for all wave conditions,
767 although they are more evident in those experiments with higher Re . In
768 addition, the differences in near bed velocity are larger upwave of the hull
769 remains than downwave. This can be attributed to the larger changes in

770 depth in this location (Figure 1c), and also to the amplification of flow
 771 velocity resulting from the erosion of the offshore sand accumulation in
 772 HEP, particularly during mean storm conditions (20%) (Table 2).

Location	$\frac{\langle U_{mo} \rangle_{E1_HEP}}{\langle U_{mo} \rangle_{E1_LEP}}$	$\frac{\langle U_{mo} \rangle_{E2_HEP}}{\langle U_{mo} \rangle_{E2_LEP}}$	$\frac{\langle U_{mo} \rangle_{E3_HEP}}{\langle U_{mo} \rangle_{E3_LEP}}$	$\frac{\langle U_{mo} \rangle_{E4_HEP}}{\langle U_{mo} \rangle_{E4_LEP}}$	$\frac{\langle U_{mo} \rangle_{E5_HEP}}{\langle U_{mo} \rangle_{E5_LEP}}$
X=194.5	20%	12%	14%	14%	10%

773 Table 2. Flow velocity increase percentage at hull remains x=194.5

774 The modification of velocity profiles is promoted by the vortex dynamics. It
 775 is observed in the LEP simulations (see for example Figure 3b upwave
 776 x=191, at $t^* = 6/9$ and $7/9$ and downwave x=198, at $t^*=2/9$ and $t^*=4/9$).
 777 This process is more obvious in HEP simulations, for instance in H2_HEP
 778 (see Figures 4b and Figure 8). At the toe of hull remains (x=198) the
 779 velocity profile is modified by the counter clockwise vortex ($t^*=4/9$ -
 780 $t^*=7/9$), increasing the near bottom velocity. Likewise, the shedding of the
 781 vortex shoreward changes the horizontal velocity profiles at x=205
 782 ($t^*=4/9$) and at x=208.5 ($t^*=6/9-7/9$).

783 The dynamics of large coherent structures (LCS) is controlled by the
 784 Keulegan-Carpenter (KC) number (Summer, 1991). LCS clearly dominate
 785 the HEP simulations due to the presence of inshore and offshore scour-crest
 786 systems, which introduce two additional areas of vortex generation. Table 3
 787 lists the KC values for the different locations prone to flow separation and
 788 vortex generation: the upwave and downwave scour-crest systems, and the
 789 hull remains. For the KC calculation, the diameter (D) was assumed as the
 790 width of the scour-crest, and the distance from the centre of the wreck site
 791 to the toe of wreck (x~197) for the hull remains.

792

	X(m)	D(m)	E1_LEP	E2_LEP	E3_LEP	E4_LEP	E5_LEP
Hull remains	195	4.1	2	6	12	15	5
	X(m)	D(m)	E1_HEP	E2_HEP	E3_HEP	E4_HEP	E5_HEP
Hull remains	195	3.7	2	5	12	16	5
Offshore scour-crest	185.2	2.3	3	9	21	26	7
Inshore scour-crest	202.7	1.2	6	7	29	40	16

793 Table 3. KC calculated from numerical experiment of the wave condition
794 tested with LEP and HEP bathymetry.

795 Flow separation does not occur at the wreck or at the offshore scour-crest in
796 simulations E1_LEP and E1_HEP, as was expected for values of $KC < 4$
797 according to Sumer (1991). K and L vortices are only observed at the
798 inshore scour crest ($KC=6$), along with the coherent structures (RC^+ and
799 RC^-), whose position and rotation match with the recirculation cell identified
800 in Figure 13a.

801 In E2_LEP, flow velocity increases at the wreck ($KC= 6$). As a result type K
802 and L' vortices are observed for E2_LEP, and the coherent structure (RC^+)
803 is identified as a recirculation cell (Figure 13c). In the E2_HEP simulation, a
804 type K' vortex is formed at the wreck ($KC= 5$) and remains attached. Vortex
805 shedding does not occur at values of $4 < KC < 7$, in agreement with Sumer
806 (1991). At the inshore scour-crest ($KC=7$), the vortex dynamics are
807 accelerated and the vortex shedding takes place as two vortex pairs; K-L
808 downwave and $M-K_2$ upwave. The $M-K_2$ pair is segregated, and the K-L pair
809 is transported initially shoreward by the counter clockwise current cell
810 (Figure 13d).

811 Although the KC increase at the wreck there is no significant variation in the
812 other LEP simulations.

813 In contrast, in E3_HEP even with the same value of KC for the wreck, the
814 absence of the offshore sand accumulation promotes the generation of a
815 type L'' vortex at the centre of the wreck site. The growth of KC =29 at the
816 inshore scour-crest does not generate changes in vortex dynamics, solely
817 producing modification in the trajectory of the M vortex that is constrained
818 by the larger clockwise current cell formed above the inshore scour pit
819 (Figure 13f).

820 In the case of the inshore breaking wave E4_HEP, a KC value of 16 is
821 calculated at the wreck, indicating a more complex dynamic as revealed by
822 the presence of a N vortex developed at the inshore scour pit, the L' vortex
823 split into smaller eddies, and the L'' vortex at the centre of the wreck site.
824 The vortex L' partition could be associated with larger turbulent shear after
825 the wave breaking process (Figure 12d). In addition the clockwise current
826 cell (Figure 13h) marks the trajectory of the M vortex and vortex shedding
827 also takes place at the offshore scour-crest system (KC=26).

828 In simulation E5_HEP, vortices are developed only at the scour-crest
829 system. The two vortex pairs at the inshore scour crest remain attached to
830 the crest, in spite of the fact that the value KC=16 is larger than the
831 supposed threshold for vortex shedding (KC=7) (Sumer, 1991).

832

833 It is important to note how vortex dynamics modifies the velocity profiles
834 and increases the turbulent shear. This is observed when mean streamwise
835 velocity (Figure 3 and Figure 4) and turbulent shear profiles (Figure 11 and
836 12) in different wave phases are compared with the position of vortices at
837 those phases (Figures 6-10). This promotes an increase in boundary layer

838 thickness (Figure 5), similar to the one that forms in the presence of sand
839 ripples when they originate from rhythmic vortices (Nielsen, 1992).

840 On the subject of turbulent shear stress, results show an important
841 increment in turbulence for the HEP morphological setting. This behaviour is
842 observed in all simulations, especially downwave of the wreck, with flow
843 velocity increase, LCS, and recirculation cells developed downwave.

844 The recirculation cells generated by the SCw are only present in the LEP
845 simulations at the toe of the wreck, with velocities lower than $0.10 \text{ m}\cdot\text{s}^{-1}$.
846 Higher velocities of steady current are associated with undertow, which is
847 markedly significant in the cases of breaking wave E4_LEP and E5_LEP
848 (Figure 13). The recirculation cells are observed in all HEP simulations,
849 particularly downwave and with larger velocities ($0.3\text{-}0.7 \text{ m}\cdot\text{s}^{-1}$) than in LEP.

850 The mean oscillatory flow brings sediment into suspension and as the
851 results have shown controls the trajectory of LCS increasing its effect in the
852 sediment transport.

853 It is remarkable the contribution of the LCS to the SCw. It can be observed
854 in the cases of E2_HEP, E3_HEP and E4_HEP (Figures 8, 9 and 10), where
855 the major LCS located in the inshore scour contributes to the residual
856 velocity as point the recirculation cell located in that area. (Figures 13d, 13f
857 and 13h). In addition, when the LCS are weak i.e. E1_HEP (Figure 6), the
858 recirculation cells can be identified by the Okubo-Weiss criteria. In that
859 case, at difference of the vortex, the RC remains during the entire wave
860 period with slight variations in its position (Figure 13a).

861 These processes modify the spatial distribution of bed shear stress on the
862 wreck and the surrounding seabed. Thus the speed up and vortex shedding

863 and its associated turbulence produce a maximum in τ/τ_c downwave of the
864 wreck, more evident in HEP simulations (Figure 14, $x \sim 200$). The increase in
865 bed shear stress caused by the vortex and the shear stress underneath the
866 vortex is clearly observable for the HEP simulation shoreward of the inshore
867 scour ($x > 202$), and at the toe of the wreck (Figure 14b). For more energetic
868 conditions (Figure 14c and Figure 14d) higher values of τ/τ_c are found in
869 LEP simulations, revealing that the influence of frictional velocity
870 amplification due to depth reduction in LEP is larger than the influence
871 caused by the effect of turbulence underneath the vortex in the HEP
872 simulations. This effect is more conspicuous upwave of the wreck, at the
873 offshore sand accumulation in LEP. Furthermore, the increase in the grid
874 size of the first computational cell above the seabed outside of region two in
875 the computational mesh (R2) (Figure 2) induces an error in the bed shear
876 stress calculation. This is observed in HEP experiments (Figure 14), where
877 τ/τ_c changes in the limit of the R2 region. However, the results are valid for
878 HEP because the relative changes induced by the increase in the grid size of
879 the first computational cell above the seabed outside of region two (R2), are
880 smaller than the changes caused by the hydrodynamic and vortex pattern.
881 On the contrary, in the case of LEP the changes promoted by the
882 hydrodynamics and the vortex pattern are not meaningful in comparison
883 with those induced by the variation in mesh size. Therefore, in the case of
884 LEP bathymetry the relative magnitude of this error with respect to the
885 spatial variation of τ/τ_c invalidates the τ/τ_c results outside the region R2.
886 Previous investigations at the wreck site (Fernández-Montblanc et al.,
887 2016), based on time-lapse bathymetric surveys and conventional
888 hydrodynamic modelling, concluded that sediment is alternatively deposited

889 and eroded at the *Fougueux* site in response to seasonal wave climate
890 variation. Thus the morphological changes observed in HEP and LEP are
891 intrinsically linked to the seasonal wave climate variation in an inter-annual
892 interactive cycle. Furthermore, a feedback mechanism occurs where the
893 geomorphological changes induce changes in the oscillatory flow velocity
894 patterns around the shipwreck. This iterative cycle can be described as
895 follows. During the mean storm after a prolonged low energy period (from
896 May to September) (H1_LEP) the friction velocity and speed of flow
897 produces the erosion of the offshore sand accumulation and the initial
898 development of the onshore scour mark. The development of the inshore
899 and offshore scour marks increases the speed of flow on the hull remains
900 (see Table 2), accelerates the vortex dynamics and the intensification of the
901 current cell, resulting in amplification of the shear stress. It occurs most
902 notably during the extreme events (H2_HEP, H3_HEP, H4_HEP and
903 H5_HEP), leading to the enhancement of sediment transport by shoreward
904 vortex shedding. Finally, during the swell-wave period (low-energy
905 conditions from May to September) asymmetry between the orbital
906 velocities beneath crests and troughs tend to drive sediment from the
907 offshore direction towards the coast producing the offshore sand
908 accumulation, partially filling partially the inshore scour mark with the
909 surrounding sediment.

910

911

912

913

914

915 **6 Conclusions**

916 The CFD simulations from the *Fougueux* site indicate that the friction
917 velocity due to oscillatory flow and flow velocity amplification are the
918 dominant physical processes in operation during the low energy period, and
919 the large coherent structure formed at the toe of the wreck initiates scour at
920 that location. During the high energy period, the relevance of turbulent
921 shear and the large coherent structure are markedly greater, and flow
922 increases at the wreck site. In addition, the recirculation cells originated by
923 steady streaming and undertow are more important in high energy periods.
924 The velocity increase of the current cell in high energy settings modifies the
925 trajectory of the shed vortex increasing its capacity of sediment transport.

926 The results confirm CFD as a valuable tool to understand the mechanisms
927 promoting scouring at shipwreck sites and other submerged structures
928 under the influence of waves. Beyond the aim of this study, the successful
929 application of a full scale CFD study in the simulation of waves and structure
930 interactions allows the behaviour of these structures in full scale and
931 realistic morphological conditions to be tested. In addition, the full scale
932 CFD application will allow the parameterization of different physical process
933 related to waves, thus avoiding the many restrictions of physical lab
934 experiments and field-based deployments during extreme conditions.

935 In summary, the full scale CFD modelling presented in this study allows
936 detailed analysis of key physical processes in coastal engineering,
937 addressing limitations inherent in traditional physical models and field
938 deployments.

939 **Acknowledgements**

940 This work has been supported by the Spanish Ministry of Economy and
941 Competitiveness, Project CTM2010-16363 (ARQUEOMONITOR).

942 **References**

943 Astley, A., Dix, J.K., Thompson, C., Sturt, F., 2014. A seventeen year, near-
944 annual, bathymetric time-series of a marine structure (SS Richard
945 Montgomery). In: Cheng, L., Draper, S. and An, H. (Eds.), Scour and
946 Erosion: Proceedings of the 7th International Conference on Scour and
947 Erosion. International Conference on Scour and Erosion. Taylor & Francis,
948 pp. 715-724.

949 Baeye, M., Quinn, R., Deleu, S., Fettweis, M., 2016. Detection of shipwrecks
950 in ocean colour satellite imagery. *J. Archaeol. Sci.* 66, 1-6.

951 Baldock, T.E., 2006. Long wave generation by the shoaling and breaking of
952 transient wave groups on a beach. *Proceedings of Royal Society A*, 462,
953 1853–1876.

954 Bates, C.R., Lawrence, M., Dean, M., Robertson, P., 2011. Geophysical
955 Methods for Wreck-Site Monitoring: the Rapid Archaeological Site Surveying
956 and Evaluation (RASSE) programme. *Int. J. Naut. Archaeol.* 40, 404-416.

957 Bergstrand, T., Godfrey, N.I., 2007. Reburial and analyses of archaeological
958 remains: Studies on the effect of reburial on archaeological materials
959 performed in Marstrand, Sweden 2002-2005. The RAAR project.

960 Kulturhistoriska dokumentationer nr 20. Bohusläns Museum: Udevalla.

961 Bozorgnia, M., Eftekharian, A., Jiin Jen, L., 2014. CFD modelling of a
962 solitary wave overtopping breakwater of varying submergence. Coastal
963 Engineering Proceedings, 1(34), waves 7.

964 Chang, K.A., Liu, P.L.F., 1999. Experimental investigation of turbulence
965 generated by breaking waves in water of intermediate depth. Phys. Fluids.
966 11, 3390–3400.

967 De Hauteclocque, G., Dix., J, Lambkin, D., Turnock, S., 2007. Flow and
968 Likely Scour Around Three Dimensional Seabed Structures Evaluated Using
969 RANS CFD, University of Southampton Ship science report, 144, 90 pp.

970 Dixen, M., Sumer, B. M., Fredsøe, J., 2013. Numerical and experimental
971 investigation of flow and scour around a half-buried sphere. Coast. Eng. 73,
972 84-105.

973 Elhmaïdi, D., Provenzale, A., Babiano, A., 1993. Elementary topology of
974 two-dimensional turbulence from a Lagrangian view point and single particle
975 dispersion. J. Fluid Mech. 257, 533–558.

976 Fernández-Montblanc, T., Quinn, R., Izquierdo, A., Bethencourt, M., 2016.
977 Evolution of a shallow water wave-dominated shipwreck site: *Fougueux*
978 (1805), Gulf of Cadiz. Geoarchaeology. 31, 487-505.

979 Gracia, F.J., Rodríguez Vidal, J., Cáceres, L.M., Belluomini, G., Benavente,
980 J., Alonso, C. (2008). Diapiric uplift of an MIS 3 marine deposit in SW
981 Spain: Implications for Late Pleistocene sea level reconstruction and
982 palaeogeography of the Strait of Gibraltar. Quat. Sci. Rev. 27, 2219-2231.

983 Higuera, P., Lara, J.L. and Losada, I.J., 2013. Realistic wave generation and
984 active wave absorption for Navier-Stokes models: Application to OpenFOAM.
985 Coast. Eng. 71,102-118.

986 Hussain, A. K. M. F., 1983. Coherent structures Reality and myth. Phys.
987 Fluids. 26, 2816-2850.

988 Isern-Fontanet, J., Font, J., García-Ladona, E., E, M., Millot, C., Taupier-
989 Letage, I., 2004. Spatial structure of anticyclonic eddies in the Algerian
990 basin (Mediterranean Sea) analyzed using the Okubo-Weiss parameter.
991 Deep Sea Res. Part II Top. Stud. Oceanogr. 51(25-26), 3009-3028.

992 Jensen, B. L., Sumer, B. M., Fredsøe, J., 1989. Turbulent oscillatory
993 boundary layers at high Reynolds numbers. J. Fluid Mech. 206, 265-297.

994 Jeong, J., Hussain, F. (1995). On the identification of a vortex. J. Fluid Mech.
995 285, 69-94.

996 Leino, M., Ruuskanen, A. T., Flinkman, J., Kaasinen, J., Klemela, U. E.,
997 Hietala, R., Nappu, N., 2011. The Natural Environment of the Shipwreck
998 Vrouw Maria (1771) in the Northern Baltic Sea: an assessment of her state
999 of preservation. Int. J. Naut. Archaeol. 40, 133-150.

1000 Le Méhauté, B., 1976. Introduction to Hydrodynamics and Water Waves.
1001 Springer-Verlag, New York.

1002 Longo, S., M. Petti, Losada, I.J., 2002. Turbulence in the swash and surf
1003 zones: a review. Coast. Eng. 45(34), 129-147.

1004 Longuet-Higgins, M.S., Stewart, R., 1960. Change in the form of short
1005 gravity waves on long waves and tidal currents. J. Fluid Mech. 8, 565-583.

1006 Mattioli, M., A. Mancinelli, Brocchini, M., 2013. Experimental investigation of
1007 the wave-induced flow around a surface-touching cylinder. J. Fluids Struct.
1008 37, 62-87.

1009 McNinch, J.E., Wells, J.I., Trembanis, A.C., 2006. Predicting the fate of
1010 artefacts in energetic, shallow marine environments: an approach to site
1011 management. *Int. J. Naut. Archaeol.* 35, 290-309.

1012 Melville, W.K., Veron, F., White, C.J., 2002. The velocity field under
1013 breaking waves: coherent structures and turbulence. *J. Fluid Mech.* 454,
1014 203–233.

1015 Menter, F. R., 1994. Two-Equation Eddy-Viscosity Turbulence Models for
1016 Engineering Applications. *AIAA Stud. J.*, (32)8, 1598-1605.

1017 Murray, S.P., 1970. Settling velocities and vertical diffusion of particles in
1018 turbulent water 1970. *J. Geophys. Res.* (75) 9, 1647-1654.

1019 Nadaoka, K., Hino, M., Koyano, k Y., 1989. Structure of the turbulent flow
1020 field under breaking waves in the surf zone. *J. Fluid Mech.* 204, 359-387.

1021 Nelson, J.M., Shreve, R.L., McLean, S.R., Drake, T.G., 1995. Role of near-
1022 bed turbulence structure in bed load transport and bed form mechanics.
1023 *Water Resour. Res.* 31, 2071-2086.

1024 Nielsen, A., Sumer, B. M., Ebbe, S., Fredsøe, J., 2012. Experimental Study
1025 on the Scour around a Monopile in Breaking Waves. *J. Waterw. Port C-
1026 ASCE.* 138(6), 501-506.

1027 Nielsen, P., 1992. *Coastal Bottom Boundary Layers and Sediment
1028 Transport.* World Scientific, 324 pp.

1029 Pasquero, C., Provenzale, A., Babiano, A., 2001. Parameterization of
1030 dispersion in two-dimensional turbulence. *J. Fluid Mech.* 439, 279-303.

1031 Quinn, R., 2006. The role of scour in shipwreck site formation processes and
1032 the preservation of wreck-associated scour signatures in the sedimentary

1033 record - evidence from seabed and sub-surface data. J. Archaeol. Sci. 33,
1034 1419-1432.

1035 Quinn, R., Boland, D., 2010. The role of time-lapse bathymetric surveys in
1036 assessing morphological change at shipwreck sites. J. Archaeol. Sci. 37,
1037 2938-2946.

1038 Quinn, R., Smyth, T.A.G., in press, Processes and patterns of flow, erosion,
1039 and deposition at shipwreck sites: a computational fluid dynamic simulation.
1040 Archaeol. Anthropol. Sci., <https://doi.org/10.1007/s12520-017-0468-7>.

1041 Rodríguez Mariscal, N.E., Rieth, E., Izaguirre, M., 2010. Investigaciones en
1042 el pecio de Camposoto: hacia la identificación del navío francés *Fougueux*,
1043 Revista PH del Instituto Andaluz del Patrimonio Histórico, 75, 94-107.

1044 Ruuskanen, A. T., Kraufvelin, P., Alvic, R., Díaz, E.R., Honkonen, J.,
1045 Kanerva, J., Karell, K., Kekäläinen, P., Lappalainen, J., Mikkola, R.,
1046 Mustasaari, T., Nappu, N., Nieminen, A., Roininen, J., Svahnback, K., 2015.
1047 Benthic conditions around a historic shipwreck: Vrouw Maria (1771) in the
1048 northern Baltic proper. Cont. Shelf Res. 98, 1-12.

1049 Saunders, R.D., 2005. Seabed scour emanating from submerged three
1050 dimensional objects: Archaeological case studies'. PhD Thesis, Department
1051 of Civil and Environmental Engineering, University of Southampton, UK.
1052 214p.

1053 Sawamoto, M., Yamashita, T., Kitmura, T., 1982. Measurements of
1054 turbulence over vortex-ripple. Coastal Engineering Proceedings; No 18
1055 (1982): Proceedings of 18th Conference on Coastal Engineering, Cape
1056 Town, South Africa, 1982.

1057 Scott, C.P., Cox, D.T., Maddux, T.B., Long, J.W., 2005. Large-scale
1058 laboratory observations of turbulence on a fixed barred beach. *Meas. Sci.*
1059 *Technol.* 16, 1903–1912.

1060 Smyth, T.A.G., Quinn, R., 2014. The role of computational fluid dynamics in
1061 understanding shipwreck site formation processes. *J. Archaeol. Sci.* 45,
1062 220-225.

1063 Soulsby, R., 1997. *Dynamics of Marine Sands: A manual Practical*
1064 *Applications*. Thomas Telford Telford, London.

1065 Stansby, P. K., Feng, T., 2005. Kinematics and depth-integrated terms in
1066 surf zone waves from laboratory measurement. *J. Fluid Mech.* 529, 279-
1067 310.

1068 Sumer, B. M., Fredsøe, J., 1990. Scour below pipelines in waves. *J. Waterw.*
1069 *Port C-ASCE.* 116(3), 307-323.

1070 Sumer, B. M., Jensen, B. L., Fredsøe, J., 1991. Effect of a plane boundary
1071 on oscillatory flow around a circular cylinder, *J. Fluid Mech.* 225, 271-300.

1072 Sumer, B., Christiansen, N., Fredsøe, J., 1993. Influence of Cross Section
1073 on Wave Scour around Piles. *J. Waterw. Port C-ASCE.* 5(477), 477-495.

1074 Sumer, B.M., Christiansen, N., Fredsøe, J., 1997. The horseshoe vortex and
1075 vortex shedding around a vertical wall-mounted cylinder exposed to waves.
1076 *J. Fluid Mech.* 332, 41-70

1077 Sumer, B.M., Whitehouse, R.J.S., Tørum, A., 2001. Scour around coastal
1078 structures: a summary of recent research. *Coast. Eng.* 44, 153-190.

1079 Sumer, B.M., Fredsøe, J., 2002. The Mechanics of Scour in the Marine
1080 Environment. World Scientific Publishing Co Pte Ltd. Advanced Series on
1081 Ocean Engineering, no. 17.

1082 Sumer, B.M., Fredsoe, J.R., Lamberti, A., Zanuttigh, B., Dixen, M., Gislason,
1083 K., Di Penta, A.F., 2005. Local scour at roundhead and along the trunk of
1084 low crested structures. Coast. Eng. 52, 995-1025.

1085 Testik, F.Y., Voropayev, S.I., Fernando, H.J.S., 2005. Flow around a short
1086 horizontal bottom cylinder under steady and oscillatory flows. Phys. Fluids.
1087 17, 47-103.

1088 Ting, F. C.; Kirby, J. T., 1996. Dynamics of surf-zone turbulence in a spilling
1089 breaker. Coast. Eng. 27(3-4), 131-160.

1090 Torres-Freyermuth, A., Lara, J., Losada, I., 2010. Numerical modelling of
1091 short and long-wave transformation on a barred beach. Coast. Eng. 57,317-
1092 330.

1093 Voropayev, S.I., Testik, F.Y., Fernando, H.J.S., Boyer, D.L., 2003. Burial
1094 and scour around short cylinder under progressive shoaling waves. Ocean
1095 Eng. 30, 1647-1667.

1096 Ward, I. A. K., Larcombe, P., Veth, P., 1999. A New Process-based Model
1097 for Wreck Site Formation. J. Archaeol. Sci. 26, 561-570.

1098 Whitehouse, R.J.S., Sutherland, J., Harris, J., 2011. Evaluating scour at
1099 marine gravity foundations. Proceeding ICE e Maritime Engineering, 164
1100 (4), 143-157.

1101 Wheeler, A. J., 2002. Environmental Controls on Shipwreck Preservation:
1102 The Irish Context. J. Archaeol. Sci. 29(10), 1149-1159.

1103 Young, D.M., Testik, F.Y., 2009. Onshore scour characteristics around
1104 submerged vertical and semicircular breakwaters. *Coast. Eng.* 56, 868-875.
1105